Master's thesis
Space physics

Statistical Properties of Cavitons and Spontaneous Hot Flow Anomalies in a Global Hybrid-Vlasov Magnetosphere Simulation

Vertti Tarvus

March 31, 2020

Supervisor(s): Dr. Lucile Turc
Dr. Markus Battarbee

Censor(s): prof. Minna Palmroth
Dr. Lucile Turc

UNIVERSITY OF HELSINKI
Master's Programme in Particle Physics and Astrophysical Sciences

P.O. Box 64 (Gustaf Hällströmin katu 2)
FI-00014 University of Helsinki

HELSINGIN YLIOPISTO — HELSINGFORS UNIVERSITET — UNIVERSITY OF HELSINKI

Tiedekunta — Fakultet — Faculty	Koulutusohjelma — Utbildningsprogram — Education programme
Faculty of Science	Master's Programme in Particle Physics and Astrophysical Sciences

Tekijä — Författare — Author
Vertti Tarvus

Työn nimi — Arbetets titel — Title
Statistical Properties of Cavitons and Spontaneous Hot Flow Anomalies in a Global Hybrid-Vlasov Magnetosphere Simulation

Opintosuunta — Studieinriktning — Study track
Space physics

Työn laji — Arbetets art — Level	Aika — Datum — Month and year	Sivumäärä — Sidoantal — Number of pages
Master's thesis	March 31, 2020	76+6 pages

Tiivistelmä — Referat — Abstract

The magnetic field of Earth interacts with the supersonic solar wind that emanates from the outer part of the Sun's atmosphere. The interaction results in the formation of Earth's magnetosphere with a bow shock and a foreshock upstream of it. Together, they form a complex system that hosts a large number of different phenomena, ranging from aurorae visible with the naked eye from Earth's surface to magnetic waves and transient structures only observable by spacecraft with in-situ measurements. In addition to spacecraft measurements, numerical simulations performed with computers have become increasingly important in space research with the constantly growing amount of available computing power.

The topic of this thesis, two types of transient structures found upstream of the bow shock in the foreshock, cavitons and spontaneous hot flow anomalies (SHFAs), are examples of phenomena that have been discovered and studied with the combination of numerical simulations and spacecraft observations. These transient types are related, as cavitons can evolve into SHFAs.

In this thesis, cavitons and SHFAs are studied with the global hybrid-Vlasov simulation Vlasiator. The transients are studied statistically in a global simulation for the first time, granting the largest statistical sample up to date. The approach taken in this study is to track individual transients in time, for which purpose a tracking algorithm was developed as a part of this thesis. With this method, the first detailed investigation of the evolution of cavitons and SHFAs is conducted.

The statistical results obtained in this work indicate that cavitons and SHFAs form in a uniform region near the bow shock. There is a distinct distance to the shock within which cavitons can become SHFAs, and it is found that SHFAs can either form independently, or evolve from cavitons. The properties of the transients are found to have some dependence on the transients' location relative to the bow shock. The propagation velocity of the transients is measured, and is found to agree with prior spacecraft observations.

Avainsanat — Nyckelord — Keywords
Bow shock, foreshock transients, cavitons, SHFAs, solar wind, magnetosphere, space physics, Vlasiator

Säilytyspaikka — Förvaringsställe — Where deposited

Muita tietoja — övriga uppgifter — Additional information

Contents

1. Introduction

1.1 The solar wind

As Earth orbits the Sun, it is constantly subjected to the solar wind, which is a continuous stream of magnetized plasma escaping from the Sun. The solar wind is a plasma, which is a state of matter made up of ionized gas. Plasma consists of ions and free electrons, containing roughly equal numbers of opposite charges in large enough amounts to appear neutral in large scales. This property is known as quasineutrality. The fundamental difference between a plasma and a neutral gas is that a plasma's behaviour arises from the long-range electrostatic interactions between individual particles, instead of mechanical collisions that dictate the behaviour of a neutral gas. Plasma is an excellent electric conductor and its dynamics are strongly affected by external magnetic fields. In the approximation of perfect conductivity, an external magnetic field embedded in a plasma is "frozen in" and is confined to move with the plasma.

The solar wind originates from the Sun's outermost atmospheric layer called the corona. The temperature in the corona is over 10^6 K, considerably higher than that of the Sun's visible surface ($\sim 6,000$ K). Due to the high coronal temperature, the plasma in the corona is accelerated to speeds in excess of the Sun's escape velocity. This allows the coronal plasma to expand supersonically (faster than the speed of sound in the medium) into the interplanetary space in the form of the solar

wind (Parker, 1958) [33].

The Sun's magnetic field is frozen into the solar wind and is dragged away from the Sun within the radial solar wind outflow. Since the solar wind flow covers the entire solar system, the magnetic field carried by the solar wind has been given the name Interplanetary Magnetic Field (IMF). The IMF has a configuration that resembles an Archimedean spiral on average. The spiral shape is due to the combination of the radial expansion of the solar wind and the IMF's footpoints' rotation with the Sun. This configuration of the IMF is known as the Parker spiral, named in honor of Eugene Parker (1927-), who predicted the configuration in 1958.

The solar wind is typically divided into two classes, which are termed the fast and slow solar wind. The fast and slow solar wind differ in flow speed, density, temperature and composition, but there is no clear limit between the two, as the solar wind is highly variable. The speed of the fast solar wind is above the median solar wind speed ($\sim$ 400 km/s), capable of reaching speeds of 750 km/s. The fast solar wind is steady, and originates from coronal holes, which are regions containing "open" magnetic field lines extending far away from the Sun. During quiet periods of solar activity, there are two large coronal holes located at the poles of the Sun. During periods of high solar activity, additional coronal holes can form all over the Sun. The slow solar wind has speeds below the median solar wind speed, and is more variable than the fast solar wind. The slow wind emanates from low solar latitudes, but all its sources are not entirely clear. Possible sources include coronal hole boundaries and coronal streamers (e.g. Cranmer et al., 2017) [8].

1.2 Earth's magnetosphere

Earth is shielded from the solar wind by its intrinsic dipolar magnetic field that extends into the space. The region in which Earth's magnetic field dominates over the IMF is defined as Earth's magnetosphere. Other planets with intrinsic mag-

netic fields also possess their own magnetospheres, namely Mercury, Jupiter, Saturn, Uranus and Neptune.

A diagram representing the basic configuration of Earth's magnetosphere is shown in Figure 1.1, by courtesy of Lang (2013) [21]. The solar wind flow compresses Earth's dipolar magnetic field on the dayside and elongates it on the nightside. The boundary that separates the magnetosphere from the solar wind plasma is called the magnetopause. At the magnetopause, the solar wind is forced to divert around the magnetosphere. However, the magnetopause is not an impenetrable barrier, and can be "opened" by a process known as magnetic reconnection. In magnetic reconnection, the connection between magnetic field lines changes, which alters the topology of the fields and accelerates plasma. At the magnetopause, reconnected field lines are carried by the solar wind towards the nightside magnetosphere. The position of the magnetopause is determined by the balance between the ram pressure of the solar wind and the magnetic pressure of Earth's intrinsic magnetic field. A typical subsolar standoff distance for the magnetopause measured from the center of Earth is around 10 Earth radii (R_E) (e.g. Shue et al., 1997, 1998) [46][47].

Earth's magnetosphere has a long "magnetotail", which extends far to the nightside of Earth. The magnetotail consists of two tail lobes, which contain magnetic field lines connected to Earth's polar regions. The northern lobe contains magnetic field lines oriented towards Earth and the southern lobe lines that are oriented away from Earth. The lobes are separated by a neutral sheet. A cross-tail electric current runs from the dawnside to the duskside between the lobes, which closes around the lobes and the magnetopause. The tail lobes contain little plasma, but a denser plasma sheet exists between the lobes. The lobe magnetic fields can also reconnect, which will result in the acceleration of plasma towards Earth and the downstream direction.

Other features of the magnetosphere include two semi-open field line regions

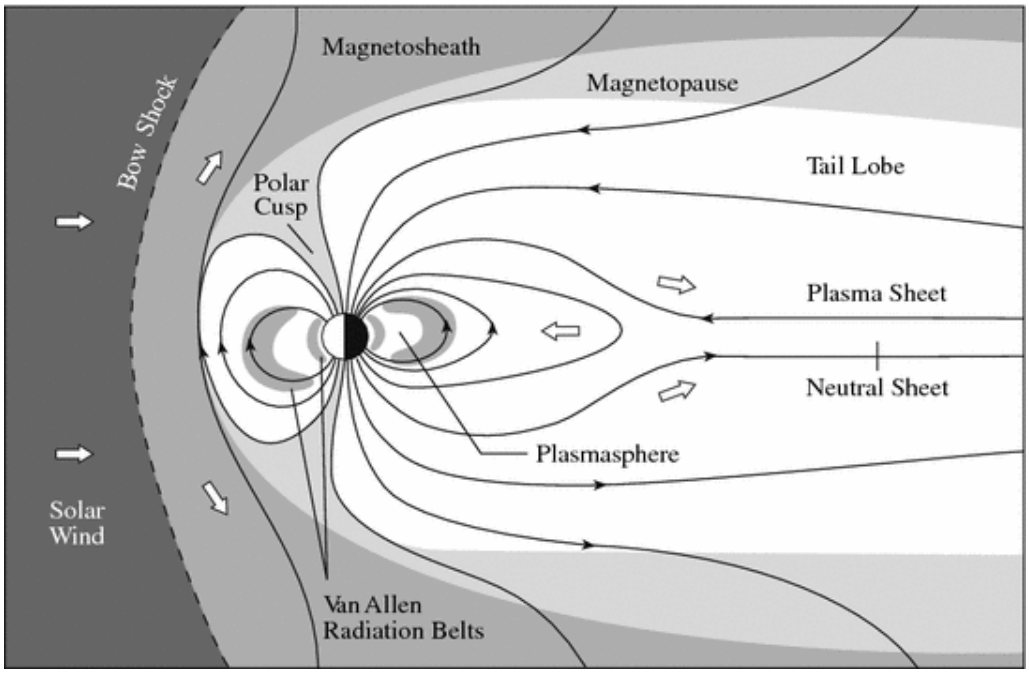

Figure 1.1: A simplified diagram of Earth's magnetosphere in the noon-midnight meridional plane. From Lang (2013) [21].

known as the polar cusps, which allow plasma to flow into Earth's ionosphere. The inner magnetosphere contains the plasmasphere and the Van Allen radiation belts. The plasmasphere contains cold, dense plasma originating from the ionosphere. The Van Allen radiation belts contain energetic particles drifting in Earth's magnetic field. In addition to the radiation belts, energetic particles in the inner magnetosphere form the ring current around Earth in the equatorial plane (not depicted in Figure 1.1) which connects to the tail current at the nightside magnetosphere.

1.3 Earth's bow shock

When a disturbance moves in a medium faster than the wave mode carrying information in the medium, a shock forms ahead of the disturbance. Shocks are characterized as thin transitions from supersonic flow to subsonic flow, accompanied by the compression and heating of the flow. The strength of a shock depends

on the Mach number, denoted by M, which is the ratio between the propagation speed of the disturbance and the wave speed in the medium. In a neutral gas, the information carrying wave mode is the sound wave, which is compressional, and has its propagation speed given by

$$v_s = \sqrt{\frac{\gamma P}{\rho}}$$

where γ is the polytropic index, P the pressure and ρ the mass density in the medium. In magnetized plasmas, such as the solar wind, additional wave modes can propagate (see e.g. book by Baumjohann and Treumann, 1997) [3]. Magnetosonic waves can create shocks in plasma, and they have two different propagation speeds given by

$$v_{ms} = \left[\frac{1}{2}(v_s^2 + v_A^2) \pm \frac{1}{2}\sqrt{(v_s^2 + v_A^2)^2 - 4v_s^2 v_A^2 \cos^2\theta}\right]^{\frac{1}{2}}$$

where the $\pm$-sign separates the slow (-) and fast (+) magnetosonic waves. In the above expression, θ is the propagation angle in respect to magnetic field and v_A is the Alfvén speed, which is given by

$$v_A = \frac{B}{\sqrt{\mu_0 \rho}}$$

where B is the magnetic field magnitude and μ_0 the vacuum permeability. The Alfvén speed is also the maximum propagation speed of the Alfvén wave, which is a transverse wave propagating in magnetic plasmas with a direction-dependent velocity $v_A \cos\theta$. Perpendicular to the magnetic field, the Alfvén mode and the slow magnetosonic mode disappear and the fast mode attains its maximum speed $\sqrt{v_s^2 + v_A^2}$ which is usually referred to as the magnetosonic speed.

As Earth's magnetosphere interacts with the supersonic solar wind, a curved bow shock forms upstream of the magnetopause (see Figure 1.1). Following the shock crossing, the compressed, heated and subsonic solar wind forms the turbulent region

between the shock and the magnetopause known as the magnetosheath. Earth's bow shock is a collisionless shock, which means that the length scale of the shock is much shorter than the mean free path of the particles in the system. Energy dissipation at a collisionless shock takes place due to wave-particle interactions instead of particle collisions (see e.g. Treumann, 2009; book by Burgess, 2015) [52][7]. The strength of a collisionless shock in a magnetized plasma is controlled by both the magnetosonic Mach number and the plasma beta, which is the ratio between plasma pressure and magnetic pressure, given by

$$\beta = \frac{P}{P_B} = \frac{nk_BT}{B^2/2\mu_0}$$

where n is the particle number density, k_B the Boltzmann constant and T the temperature. β controls the importance of the magnetic field and the level of turbulence at the shock (e.g. Paschmann and Daly, 1998) [39].

The solar wind flow upstream of Earth's bow shock has magnetosonic and Alfvén Mach numbers usually in the range $2 \leq M_{ms} \leq 7$ and $2.5 \leq M_A \leq 12$ (Winterhalter and Kivelson, 1988) [58]. Since the flow speed exceeds the fast magnetosonic speed, the wave mode responsible for Earth's bow shock is the fast magnetosonic wave and the shock is categorized as a "fast" shock. In a fast shock, the magnitude of the magnetic field tangential to the shock increases downstream, whereas the magnetic field component normal to the front remains unchanged. Conversely, at a "slow" shock the magnitude of the tangential component decreases.

1.4 The foreshock region

The properties of a collisionless shock are also controlled by the orientation of the magnetic field in respect to the shock front. Conventionally, Earth's bow shock is divided into two regions based on the angle θ_{Bn} between the magnetic field direction

and the normal of the shock. The portion of the shock in which $\theta_{Bn} < 45°$ is called quasi-parallel, and correspondingly the portion in which $\theta_{Bn} > 45°$ is called quasi-perpendicular. Figure 1.2 (by Treumann and Scholer, 2001) [53] shows a typical example of the geometry between the IMF and Earth's bow shock, including some of the features associated with different portions of the shock. The quasi-parallel and quasi-perpendicular regions are found at the upper and lower parts of the diagram, respectively.

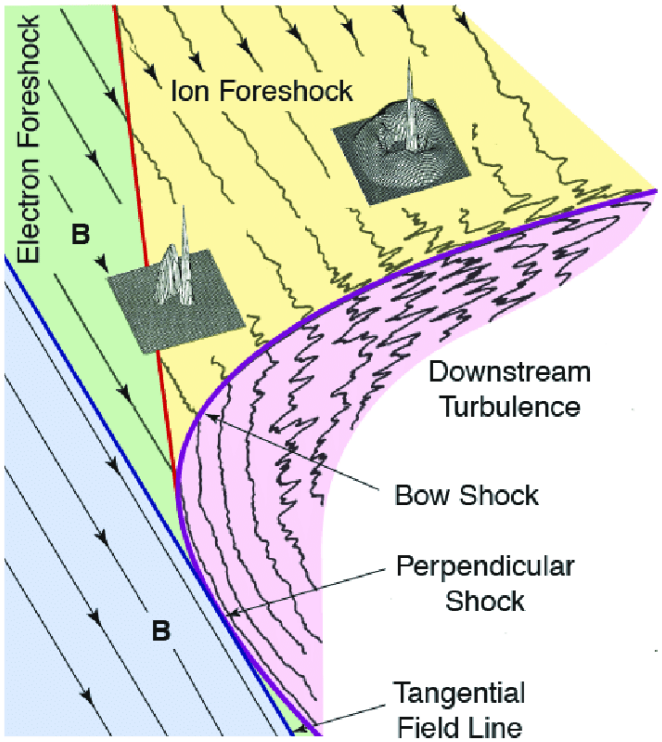

Figure 1.2: A diagram showing the geometry of Earth's bow shock and the foreshock region. The field lines of the IMF are shown with arrowed lines labelled "**B**". The 2D distributions depict the typical ion velocity distributions at their respective locations. From Treumann and Scholer (2001) [53].

Part of the kinetic energy at Earth's bow shock is dissipated by reflecting solar wind electrons and ions back to the upstream direction. This occurs above a certain "critical" Mach number, where wave-particle interactions can not solely dissipate all of the incoming energy at the shock (e.g. Treumann, 2009) [52]. The critical

Mach number depends on the upstream plasma beta and θ_{Bn}. For typical solar wind conditions, the value is between 1 and 2 (Edmiston and Kennel, 1984) [10]. At the IMF lines which connect to the bow shock, beginning from the tangential field line ($\theta_{Bn} \leq 90°$, right of the blue line in Figure 1.2), electrons and ions reflected by the bow shock are able to propagate far upstream from the bow shock. The reflected backstreaming particles interact with the incoming solar wind flow, giving rise to instabilities, which in turn can generate waves (e.g. Russell and Hoppe, 1983) [41]. The resulting turbulent region located upstream of the quasi-parallel bow shock is known as the foreshock, which is permeated by various types of ultra low frequency (ULF, f$\sim$ 1 mHz-10 Hz) waves and transient structures (Eastwood et al., 2005) [9].

The foreshock is typically divided into two regions, which are known as the electron and ion foreshocks. These regions are shown in Figure 1.2 in green and yellow color, respectively. In the electron foreshock, only backstreaming electrons are observed. Beginning from the ion foreshock boundary (red line) backstreaming ions are also found. The separation of the electron and ion foreshock boundaries arises from the different speeds of the particles. Both the reflected electrons and ions are subjected to the convection electric field of the solar wind (given by $\mathbf{E} = -\mathbf{v_{SW}} \times \mathbf{B}$), which causes them to drift in addition to the field-aligned motion with a speed

$$\mathbf{v_{E\times B}} = \frac{\mathbf{E} \times \mathbf{B}}{B^2}$$

perpendicular to the IMF field lines, independent of the mass, charge and velocity of the particles. Thus, the fastest/most energetic particles are least deviated from their original propagation direction, and are found closest to the foreshock edge. Figure 1.3 visually demonstrates how the $\mathbf{E}\times\mathbf{B}$-drift affects the movement of backstreaming ions. Due to the drift, the position of the ion foreshock boundary is shifted away from the IMF direction.

The grey 2D distributions displayed in Figure 1.2 depict the different basic

ion populations found in the foreshock (Paschmann et al., 1981; Russell and Hoppe, 1983; Kempf et al., 2015) [38][41][20]. The distributions are in the velocity space (in the 2D-plane of the figure), showing the relative amount of particles moving with different velocities at that position in the ordinary space. The velocity distributions in Figure 1.2 are centered around sharp peaks which correspond to the solar wind core population moving with a uniform velocity.

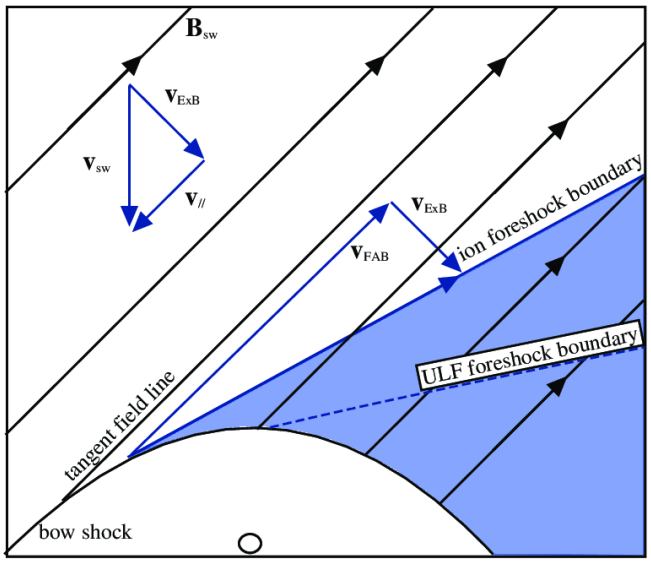

Figure 1.3: The boundaries of the ion foreshock for a typical IMF orientation. $\mathbf{v}_{sw}$ is the solar wind velocity vector and $\mathbf{v}_{FAB}$ is the velocity vector of the field aligned backstreaming particles. The particles $\mathbf{E}\times\mathbf{B}$-drift with the velocity $\mathbf{v}_{\mathbf{E}\times\mathbf{B}}$. ULF waves are observed below the ULF foreshock boundary. From Eastwood et al. (2005) [9].

The left-side distribution of Figure 1.2 shows a field-aligned beam (FAB), where the solar wind core is accompanied by a broader and smaller peak that is directed upstream along the field lines. This corresponds to a population of ions streaming away from the bow shock as a narrow beam along the IMF. FABs are observed close to the ion foreshock boundary. The right-side distribution of Figure 1.2 shows a diffuse population, which is nearly isotropic (velocities directed in all directions) and contains a broad ion energy spectrum surrounding the solar wind core. Diffuse

ions are observed deep in the ion foreshock, upstream of the quasi-parallel shock. The diffuse population is distinct from the FAB, and FABs do not evolve into diffuse populations (Fuselier, 1995) [12]. Multiple different mechanisms for the generation of diffuse ions involving shock reflection/acceleration and scattering have been suggested (see Wilson, 2016 and the references therein) [56]. Between the FAB and the diffuse population, there exists an intermediate population (not shown in Figure 1.2), which resembles the FAB but has a broader crescent-shaped beam. Different from the diffuse population, the intermediate population contains only backstreaming ions accompanying the solar wind core. There are also populations that gyrate together around magnetic field lines and do not have field-aligned peaks in their distributions. These populations are typically gyrotropic (a ring-shaped distribution around the magnetic field direction) close to the bow shock and gyrophase-bunched (a partial ring distribution/non-zero mean velocity perpendicular to the magnetic field direction) further away from it (Fuselier et al., 1986) [13]. Gyrating ions are found in the intermediate region or in a thin layer separating the FAB and intermediate regions (Meziane and d'Uston, 1998) [24].

The FAB region is not associated with ULF waves (Paschmann et al., 1979) [37]. Deeper in the ion foreshock, there exists a ULF foreshock boundary (depicted in Figure 1.3) that separates the region where ULF wave activity takes place from the FAB region. The most common ULF waves are "30 second waves", which derive their name from their typical period. At Earth they appear as quasi-monochromatic, transverse and circularly polarized waves near the ULF foreshock boundary. The 30 second waves are intrinsically right-hand polarized, and propagate sunwards in the solar wind rest frame. In the spacecraft frame, they are observed with left-hand polarization since they are convected by the solar wind. Deep in the ULF foreshock, 30 second waves appear as highly compressional and steepened "shocklets" (Greenstadt et al., 1995) [14]. Shocklets are often associated with high-frequency

discrete wave packets in their steepening edges. Other wave types observed in the ion foreshock include 1 Hz waves, 3 second waves and 10 second waves (e.g. Wilson, 2016) [56].

1.5 The characteristics of cavitons and spontaneous hot flow anomalies

In addition to ULF waves, the ion foreshock houses various transient structures. This thesis is concerned with two types of foreshock transients, namely foreshock cavitons (Blanco-Cano et al., 2009) [6] and spontaneous hot flow anomalies (SHFAs) (Zhang et al., 2013; Omidi et al., 2013) [59][31]. Other transients found in the foreshock include foreshock cavities, density holes, hot flow anomalies (HFAs, where SHFAs derive their name from), magnetic bubbles and short large-amplitude magnetic structures (SLAMS).

Cavitons and SHFAs are observed as simultaneous, roughly equal depressions of plasma density and magnetic field magnitude, bounded by overshoots in the same parameters. They are found in the diffuse ion region of the foreshock, are surrounded by ULF waves and are carried by the solar wind towards the bow shock. The ion distribution inside cavitons is similar to their surroundings, while SHFAs contain notably larger amounts of suprathermal ions inside them. As a consequence, the temperature inside SHFAs is increased and the solar wind flow slowed down and deflected. Cavitons do not exhibit these properties, which sets them apart from SHFAs. However, cavitons and SHFAs are related, as cavitons can evolve into SHFAs when they fill up with backstreaming suprathermal ions (Omidi et al., 2013; Blanco-Cano et al., 2018) [31][4]. SHFAs surviving to the bow shock can cause the shock to erode (Blanco-Cano et al., 2018). Omidi et al. (2014b, 2016) [28][26] proposed that SHFAs can also form transients in the magnetosheath, such as

magnetosheath filamentary structures (MFS) (Omidi et al., 2014b), magnetosheath cavities (Katırcıoğlu et al., 2009) [19] and high speed jets (e.g. Hietala et al., 2009) [15], or that they could cause motion of the magnetopause.

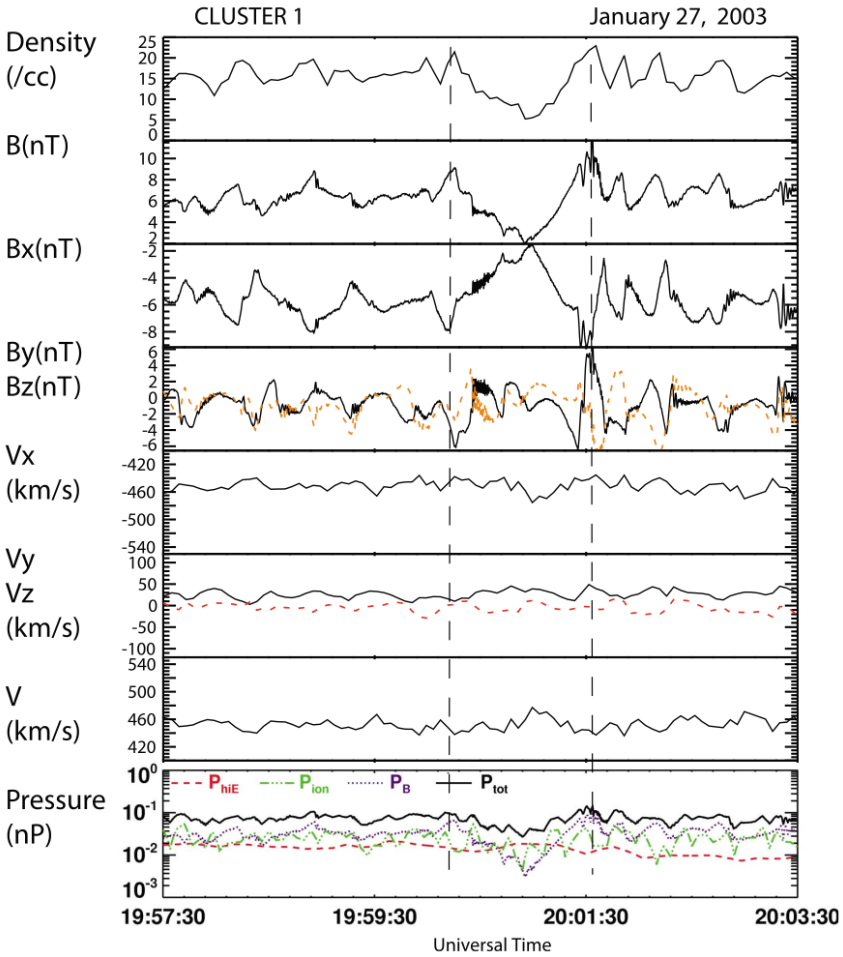

Figure 1.4: A caviton observed by Cluster on 27.1.2003 with an IMF cone angle $\theta_{vB} \sim 9°$. The caviton is shown between two vertical dashed lines. Bz and Vz are shown with orange and red dashed lines, respectively. P_{hiE}, P_{ion}, P_B and P_{tot} show the suprathermal ion pressure, solar wind pressure, magnetic pressure and the total pressure separately. The duration of this caviton is ∼79 s. From Blanco-Cano et al. (2011) [5].

Figure 1.4 shows an example of a caviton observed by the Cluster spacecraft. The data is shown in the GSE (Geocentric Solar Ecliptic) coordinate system where the x-axis is directed from Earth to the Sun, the z-axis is directed north of the ecliptic and the y-axis points to the dusk. In the figure, clear depressions are seen

in the density and magnetic field magnitude, which are deeper and more extended than the surrounding ULF fluctuations. The depressions are bounded by rims in which the parameters are enhanced. No significant changes in the bulk flow speed and the total pressure are observed inside the caviton. Near the left edge of the caviton, a "train" of high frequency waves can be seen. Such features have been observed occasionally inside or in the vicinity of cavitons in both spacecraft data and simulations (Blanco-Cano et al., 2011; Kajdič et al., 2011) [5][18].

A similar example of an SHFA observed by the THEMIS spacecraft is displayed in Figure 1.5. The data is shown in the GSM (Geocentric Solar Magnetospheric) coordinate system which is similar to the GSE system, but has the z-axis replaced with a projection of Earth's magnetic dipole axis to the yz-plane of the GSE system. In panel 2e, the presence of backstreaming suprathermal ions can be seen in the ion energy spectrum above the solar wind core population located at $\sim$1 keV. Inside the SHFA, similar to the caviton presented in Figure 1.4, depressions of density and magnetic field magnitude are observed alongside with rims where the parameters are enhanced. Additionally, the SHFA is characterized by a significantly slowed and deflected bulk flow speed and increases in the ion temperature and total pressure.

The initial study of cavitons was made by Lin (2003) [22] with a 2D hybrid (discrete particle protons, fluid electrons) simulation. Further computational studies were made by Lin and Wang (2005) [23] with a similar 3D simulation, and Blanco-Cano et al. (2009) [6], who also confirmed the existence of cavitons with observations from the Cluster spacecraft. Blanco-Cano et al. (2009) were also the first to use the term "caviton"[1] to distinguish the transient type from other similar, earlier found transient types associated with density and magnetic field depressions.

[1]The studies by Lin (2003), and Lin and Wang (2005) referred to cavitons as "diamagnetic cavities".

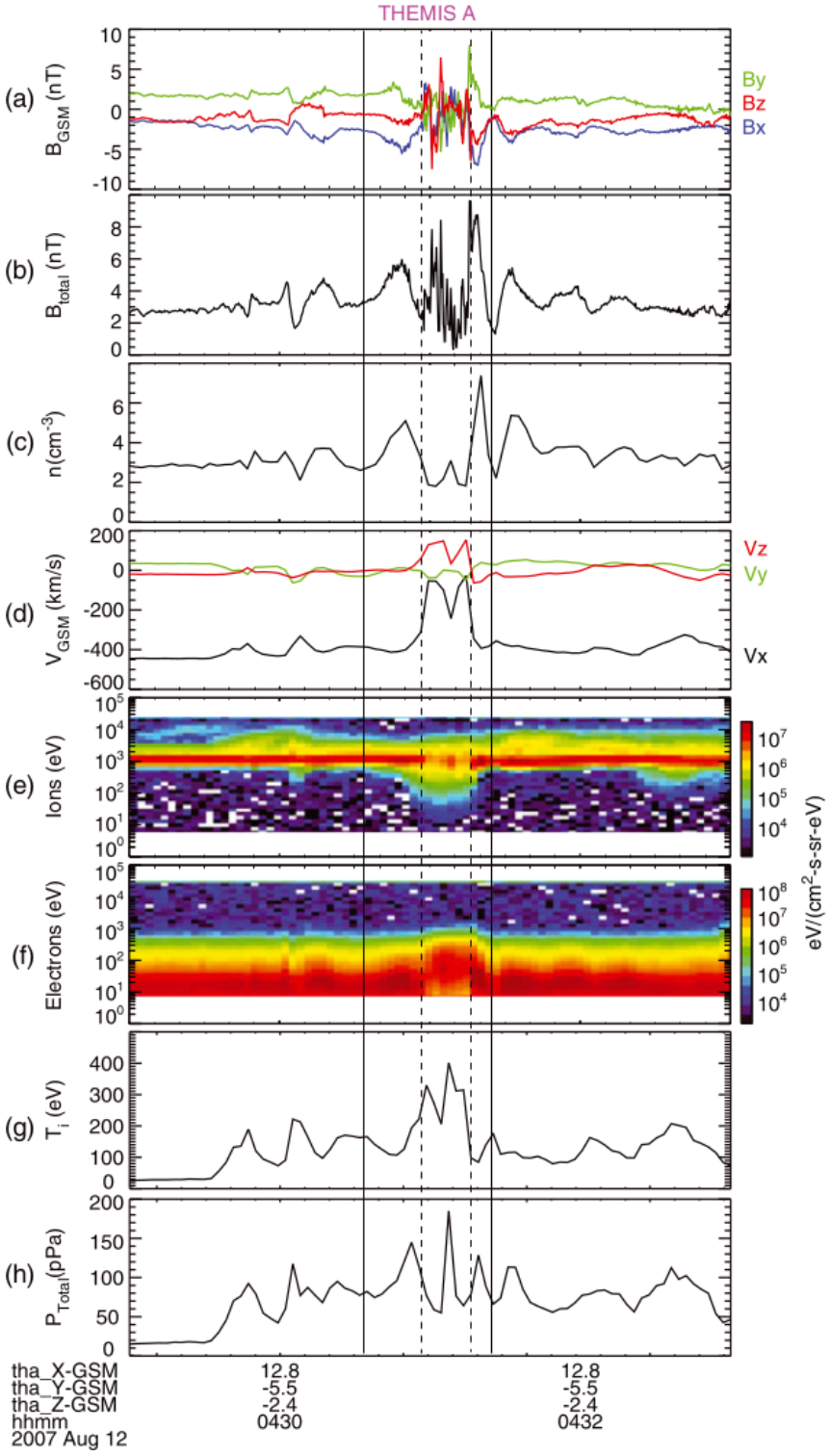

Figure 1.5: An SHFA observed by THEMIS on 12.8.2007. From top to bottom: (a): the magnetic field components, (b): magnetic field magnitude, (c): ion density, (d): bulk flow velocity components, (e) and (f): Energy spectra of ions and electrons, (g): ion temperature, (h): total pressure. The solid vertical lines mark the extent of the observed event and the dashed lines highlight the interval of significant flow deflection. From Zhang et al. (2013) [59].

In 2D simulations, the shape and extent of cavitons and SHFAs is more evident than in spacecraft observations. Figure 1.6 shows a snapshot of a hybrid simulation performed by Omidi et al. (2013) [31], where cavitons can be found. In 2D, cavitons are seen as localized density depressions deep in the foreshock, with varying sizes and irregular shapes. It can be seen that the ion foreshock is simultaneously permeated by several cavitons.

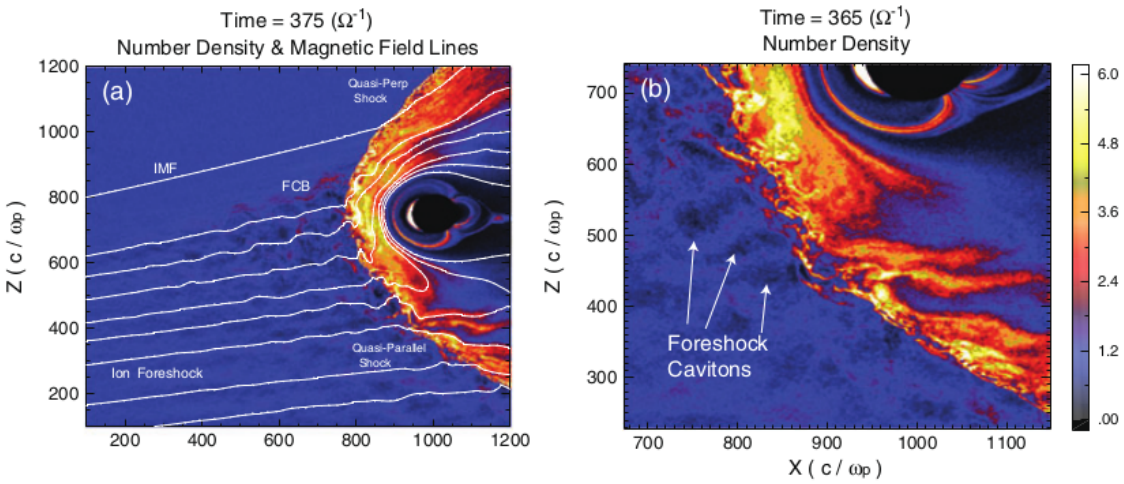

Figure 1.6: Cavitons as seen in a hybrid simulation. (a): A global view showing the number density and the magnetic field lines. The number density is normalized to the solar wind value and the cavitons are seen as dark localized density depressions. (b): A close-up view showing cavitons near the bow shock. "FCB" refers to a foreshock compressional boundary, separating turbulent and laminar regions of the foreshock (e.g. Omidi et al., 2009b) [29]. From Omidi et al. (2013) [31].

The numerical studies of Lin, Lin and Wang and Blanco-Cano et al. established that cavitons have density and magnetic field depressions of around ∼50% of ambient values, and are of the order of ∼1 R_E in size. Analysis of Cluster observations by Kajdič et al. (2011) [18] showed that cavitons found in Earth's foreshock have irregular shapes and propagate sunwards in the solar wind rest frame, but are convected back to the bow shock within the solar wind flow.

Kajdič et al. (2013) [16] performed a statistical study of cavitons with Cluster, and found that cavitons can appear with various solar wind and IMF conditions.

They reported well-correlated density and magnetic field depressions inside cavitons, with decreases from ambient values ranging between 20%-85% (a lower limit of 20% was used as a criterion) and the average decreases being 52% for the density and 47% for the magnetic field. The average duration of a caviton in spacecraft data was found to be 65 s and the average extent 4.6 R_E. Another statistical study with Cluster data by Kajdič et al. (2017) [17] added SHFAs to the caviton dataset from Kajdič et al. (2013). They found that SHFAs have very large depressions in the density and magnetic field magnitude, with the average decreases of 90% from ambient values. Their durations were found to be similar to cavitons, of the order of ∼1 min. SHFAs were observed up to 6 R_E from the bow shock and cavitons up to 9 R_E. Omidi et al. (2014a) [30] numerically studied the dependencies of SHFAs' occurrence and properties on the Alfvén Mach number of the solar wind, and the cone angle (angle from the Sun-Earth line) of the IMF. The study suggested that the SHFA formation rate increases with the Alfvén Mach number, as do the sizes, flow deflections and temperatures of SHFAs. SHFAs were found to form at all cone angles when $M_A \gtrsim 3$.

The proposed formation mechanism for cavitons involves two different types of ULF waves evolving non-linearly (Omidi, 2007; Blanco-Cano et al., 2009) [25][6]. The first one is a weakly compressional circularly polarized wave propagating parallel to the magnetic field, exhibiting either right- or left-handed polarization. The other one is a compressional, linearly polarized fast magnetosonic wave that propagates at a highly oblique angle in respect to the magnetic field, known as a FLO (fast linearly polarized oblique) wave. When both of these waves steepen and interact with each other, they lose coherence and their wavefronts merge, which leads into the formation of localized and simultaneous depressions of plasma density and magnetic field magnitude.

Cavitons and SHFAs are distinct from other similar foreshock transients as-

sociated with density and magnetic field depressions. HFAs (Schwartz et al., 1985) [44] are the namesake of SHFAs, which form when a tangential discontinuity/current sheet in the IMF interacts with the bow shock. The term "spontaneous" in the case of SHFAs arises from their resemblance to HFAs and their formation in the absence of solar wind discontinuities (Zhang et al., 2013) [59]. The formation of an HFA requires that an IMF discontinuity is connected to the bow shock, and that the convection electric field of the solar wind points towards the discontinuity. Under such circumstances, the electric field can channel bow shock-reflected suprathermal ions towards the discontinuity and confine them (Thomsen et al., 1993) [51]. The confined ions cause expansion, resulting in a region with significantly heated and deflected flow, and decreased density and magnetic field magnitude bounded by a rim where the quantities are enhanced. The sizes of HFAs inferred from observations range between ∼2-3 R_E (Facskó et al., 2009) [11]. As HFAs are found in conjuction with IMF discontinuities, they are unrelated to cavitons and SHFAs.

Foreshock cavities (e.g. Thomas and Brecht, 1988; Sibeck et al., 2002) [50][49] and density holes (Parks et al., 2006; Parks et al., 2007) [36][35] are other examples of transients associated with simultaneous depressions of plasma density and magnetic field magnitude. Foreshock cavities form at isolated bundles of IMF lines connected to the quasi-parallel bow shock. The pressure of suprathermal ions streaming from the shock along these lines causes them to expand, pushing the surrounding plasma and creating a cavity with compressed edges (Schwartz et al., 2006) [45]. Cavities only have suprathermal ions inside them, and have a large thermal pressure compared to their surroundings. Cavitons can be recognized as a separate structure type, as they have similar thermal pressure as in their surroundings, and are always surrounded by ULF waves, which is not necessarily always the case with foreshock cavities. Different to HFAs and SHFAs, foreshock cavities do not show significant heating or flow deflection (Sibeck et al., 2002) [49]. Furthermore, it was suggested

by Sibeck et al. (2008) [48] that some foreshock cavity observations could result from the movement of the ion foreshock, causing a spacecraft to briefly encounter the ion foreshock boundary and observe a "cavity". Density holes exhibit deflection of solar wind flow and plasma heating in addition to density and magnetic field depressions. They are much smaller than cavitons, and can have non-equal levels of density and magnetic field depressions, whereas inside cavitons the depressions are of similar amplitude (Parks et al., 2006; Blanco-Cano et al., 2011) [36][5].

Foreshock bubbles (Omidi et al., 2010) [27], like HFAs, form in the presence of an IMF discontinuity. One suggested mechanism for foreshock bubble formation is the following (e.g. Archer et al., 2015) [1]; When there is a rotational discontinuity in the IMF that increases the angle between the IMF and the Sun-Earth line in the upstream direction, backstreaming suprathermal ions passing through the discontinuity will experience a stronger convection electric field upstream of it, and $\mathbf{E} \times \mathbf{B}$-drift back towards the discontinuity. This would lead to a build-up and heating of suprathermal ions upstream of the discontinuity, which in turn leads to expansion of plasma. The result is a foreshock bubble, a structure similar to an HFA with a hot and depleted core, also capable of driving shocks in the upstream direction. A key difference between foreshock bubbles and HFAs is that HFAs require an IMF discontinuity to intersect with the bow shock, while foreshock bubbles don't. Moreover, foreshock bubbles only form on the upstream side of IMF discontinuities and can be notably larger in size than HFAs (Turner et al., 2013) [54].

Besides cavitons, SLAMS (Schwartz and Burgess, 1991; Schwartz et al., 1992) [42][43] are another type of transient structure forming from ULF waves. SLAMS are observed simultaneously with diffuse ions, but are different in nature compared to cavitons. They are the result of the steepening of a single type of ULF wave, and are characterized as short, localized bursts of intense magnetic field fluctuations.

1.6 The outline of this work

The goal of this work is to conduct a statistical study of foreshock cavitons and SHFAs with Vlasiator, a global hybrid-Vlasov magnetospheric simulation developed at the University of Helsinki. A previous study of cavitons and SHFAs with Vlasiator has been conducted by Blanco-Cano et al. (2018) [4]. Figure 1.7 shows a snapshot of Earth's magnetosphere in the Vlasiator simulation run studied in this work. The simulation run is conducted in the noon-midnight meridional plane, depicting a similar cut of the magnetosphere as the schematic in Figure 1.1. The bow shock is seen as a clear jump in density, with a smooth surface in the quasi-perpendicular shock (upper part) and an irregular, rippled surface in the quasi-parallel shock (lower part). The foreshock is found upstream of the quasi-parallel shock, where density and magnetic field fluctuations can be seen. Cavitons and SHFAs found in the foreshock are highlighted in black (no distinction made between cavitons and SHFAs).

In the simulation run, the foreshock is permeated by a number of cavitons and SHFAs at all times, with constant formation of new ones and disappearance of old ones. The transient structures also interact with each other, by merging together or by splitting up into smaller structures. For the purposes of the statistical study carried out in this work, a tracking algorithm was developed, which is capable of following individual structures and detecting the interactions between them. The algorithm constructs a history for each tracked structure, and allows viewing any point of their evolution and their interactions with other structures.

The topics that are examined in this thesis include the formation and occurrence of cavitons and SHFAs in the foreshock, their physical properties such as the depth of their density and magnetic field depressions, and their evolution and propagation characteristics. The thesis is divided into sections in the following order; The methods used in this work are presented in Chapter 2, where Vlasiator is briefly introduced, the detection method of cavitons and SHFAs is presented and the princi-

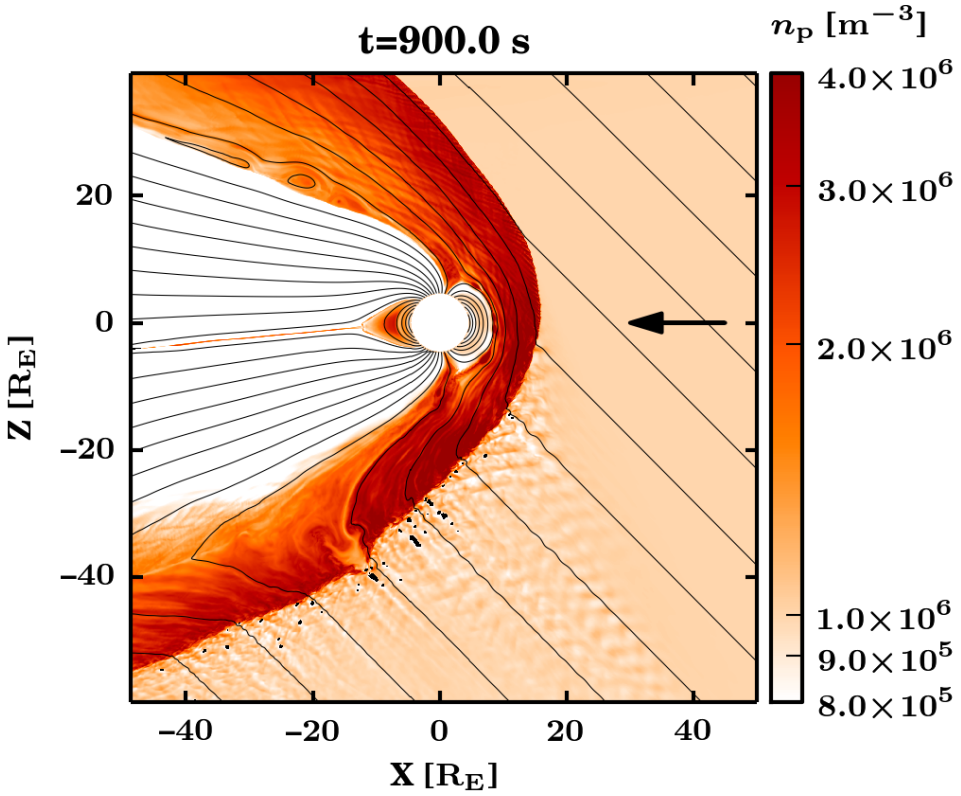

Figure 1.7: Earth's magnetosphere as seen in a Vlasiator simulation run in the noon-midnight meridional plane. The coloring shows the proton number density n_p in particles/m^3. The solar wind flows from the right, with its direction depicted by a thick arrow. Magnetic field lines are shown with thin black lines. Earth is located at the origin, and the inner boundary of the simulation corresponds to a perfectly conducting ionosphere. Cavitons and SHFAs found in the foreshock are highlighted in black in the lower part of the figure.

ple of the tracking algorithm developed for this work is detailed. Chapter 3 presents the results. Chapter 4 contains further discussion about the results. In Chapter 5, a summary alongside the conclusions is given. A pseudocode implementation of the tracking algorithm developed for this work can be found in Appendix A at the end of this thesis.

2. Methods

2.1 Vlasiator

Vlasiator is a global hybrid-Vlasov code used for simulating Earth's magnetosphere and the plasma environment surrounding it (von Alfthan et al., 2014; Palmroth et al., 2018) [55][32]. In the hybrid-Vlasov approach, each ion species s is modelled using a position-velocity distribution function $f_s(\mathbf{r}, \mathbf{v})$, which yields the particle number density $n_s(\mathbf{r})$ when integrated over the velocity space and the total number of particles N_s when integrated over both the position space and the velocity space. The hybrid-Vlasov approach does not model electrons as a distribution, but instead models them as a charge-neutralizing fluid. The ion distribution function evolves in time according to Vlasov's equation, given by

$$\frac{\partial}{\partial t} f_s(\mathbf{r}, \mathbf{v}, t) + \mathbf{v} \cdot \frac{\partial}{\partial \mathbf{r}} f_s(\mathbf{r}, \mathbf{v}, t) + \frac{q}{m}(\mathbf{E} + \mathbf{v} \times \mathbf{B}) \cdot \frac{\partial}{\partial \mathbf{v}} f_s(\mathbf{r}, \mathbf{v}, t) = 0$$

where q and m are the charge and mass of the ion species s, and $\mathbf{E}$ and $\mathbf{B}$ are the electric and magnetic fields. Vlasov's equation describes the change of f_s in time (first term), which occurs due to translation/advection (second term) and acceleration (third term). Collisions between particles are neglected.

In Vlasiator, the distribution function for ions is 6-D, being 3-D in both the ordinary position space and the velocity space. The simulation runs up to date have been carried out using a 2-D position space and a 3-D velocity space. A Cartesian

mesh is used for both spaces. The electromagnetic fields in Vlasov's equation are solved using Maxwell's equations, where the Darwin approximation of Ampère's law is used (neglecting the displacement current). The resulting system of equations is closed with Ohm's law including the Hall term. The system is advanced in time by using Strang splitting, which separates the translation and acceleration terms of Vlasov's equation into separate operators. A leapfrog scheme is used, in which the translation and acceleration of the distribution function and the propagation of the electromagnetic fields take turns.

2.2 Identifying cavitons and SHFAs

In this work, cavitons are considered to be structures in the foreshock with densities and magnetic field magnitudes less than 80% of ambient solar wind values. These criteria were first used in a statistical study of cavitons conducted with Cluster data by Kajdič et al. (2013) [16]. The same criteria were also used in a previous simulation study done with Vlasiator by Blanco-Cano et al. (2018) [4]. SHFAs are identified as cavitons which have β>10 in at least 60% of their cells. This criterion was also used in Blanco-Cano et al. (2018). The categorization of the data is discussed in more detail in Section 2.4. For the rest of this chapter, non-categorized cavitons and SHFAs will be both referred to as "structures".

As a first step to finding individual structures, all spatial simulation cells fulfilling the caviton criteria in the foreshock are identified in a simulation run at each timestep of the studied time interval. In order to exclude cells located inside the bow shock/magnetosphere, two 4th order polynomials are used to evaluate the position of the bow shock. These polynomials give the position of the bow shock in the direction of the Earth-Sun line (x), as a function of position on the perpendicular axis (z, polar plane). The polynomial is calculated by finding a jump in the solar wind density along the x-axis, for each row of the simulation box. The first polynomial fit

is made for the first timestep of the studied interval, and the other one is similarly made for the last timestep. With these polynomials, the bow shock position at a single timestep in time interval (t_0,t_1) is then acquired by interpolation as

$$x_{BS}(z,t) = \Big(1 - \frac{t-t_0}{t_1-t_0}\Big) * x_{BS}(z,t_0) + \Big(\frac{t-t_0}{t_1-t_0}\Big) * x_{BS}(z,t_1)$$

Using this model, all cells fulfilling the caviton criteria downstream of bow shock are removed.

When all the cells that fulfill the caviton criteria in the foreshock have been identified, they are sorted into separate structures at each timestep. This is done by iterating through the list of cells, checking if a cell has already been visited, and finding all cells connected to that cell. All cells connected to a single cell are found by starting from the first cell, finding cells adjacent to it, and conducting the same search for all newly found adjacent cells. When all connected cells are found, an independent structure is identified and the search moves on to the next cell that hasn't yet been visited. After all the independent structures have been found at all timesteps, the next step is to track them in time.

2.3 Techniques for tracking structures

In this section, a scheme is described for the purpose of tracking structures, developed for this work. The goal is to be able to identify individual structures and follow their evolution from their formation to the point where they disappear. Another goal is to be able to recognize merging and splitting events occurring between structures to get a clear picture of their evolution.

The principle of the tracking scheme described in this section is such that smaller structures split/merge from/into larger structures. The scheme can be separated into two tasks, which are repeated between each timestep of the tracking

interval:

1. Resolving relations between structures at consecutive timesteps
2. Tracking evolving structures and constructing a history for each tracked structure

The framework for fulfilling these tasks will be presented in the next two subsections. The methods included in this scheme are fairly universal, and can be also used to track other structures apart from cavitons/SHFAs, as long as they are identified/sorted in similar manner as explained in the previous section.

2.3.1 Resolving relations between structures

First, it is necessary to define what "relations" between structures mean. Structures at consecutive timesteps are considered to be related if their areas have enough overlap. Here it is assumed that structures move at relatively low speeds, since very fast-moving structures can have no overlap at all. "Enough" overlap cannot be quantified in a definitive way, but it should be chosen to be relatively small in order to ensure that faster structures can be tracked. However, if the required amount of overlap is very small, tracked structures might behave strangely. Conversely, too large setting for the overlap will result in a bad detection rate for moving/deforming structures. The amount of overlapping between two structures is here evaluated by counting the number of overlapping cells and then dividing it by the cell count of the smaller of the two structures. If this ratio exceeds a fixed percentage, the structures are considered to be related.

There are different types of relations between structures, which are explicitly defined on the next page. Alongside with the definitions, a set of logical rules that uniquely determine the relations between structures are presented. These relation types represent the different evolutionary steps structures can go through, such as

translation, splitting from another structure, or merging into another structure. In addition to these, a less intuitive but possible relation exists, which is here termed as "partial splitting". Partial splitting represents cases where a part of a structure splits off and immediately merges into another structure. Partial splitting is ignored in the tracking scheme used in this work, but is introduced here for completeness' sake.

1. Possible relations between structures at consecutive timesteps are:
   (a) Translate (T): Structure at timestep N becomes a structure at timestep N+1
   (b) Merge (M): Structure at timestep N becomes a part of another structure at timestep N+1
   (c) Split (S): Structure at timestep N+1 is separated from a translating or merging structure
   (d) Partial split (P): A part of a translating or merging structure splits off and merges into a structure at timestep N+1
2. Structure X at timestep N and structure X', the largest structure related to X at timestep N+1, are related in either way:
   (a) If X is the largest structure related to X', X translates into X'
   (b) If X is not the largest structure related to X', X merges into X'
3. Structure Y' at timestep N+1, which is related to X but is not X', is related to X in either way:
   (a) If X is the largest structure related to Y', Y' is split from X
   (b) If X is not the largest structure related to Y', Y' is partially split from X

Visualizations of the four relation types defined above are shown in Figure 2.1. The top illustration in Figure 2.1 depicts translation, splitting and merging. There, B is the largest structure at timestep N, and B' is the largest structure at timestep N+1. B translates to become B' as per rule 2 a) in the above definitions. Structure A merges into B', and structure C' splits from B, as dictated by rules 2 b) and 3 a), respectively.

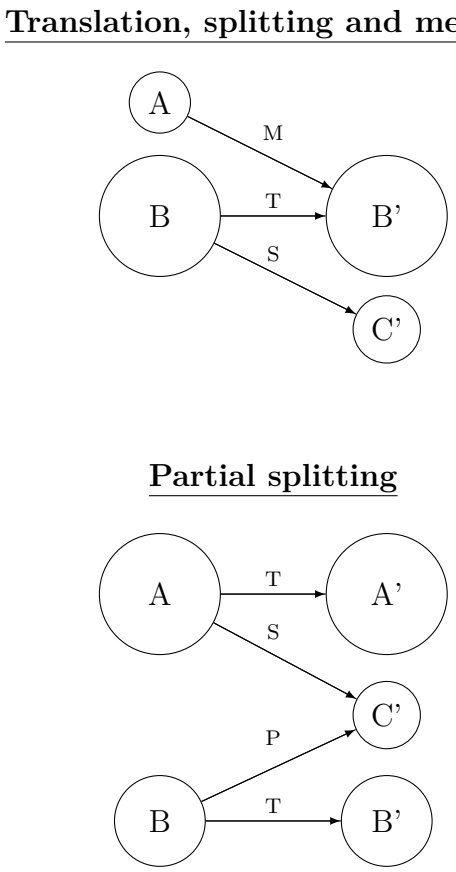

Figure 2.1: Illustrations of the different relation types between structures, as defined above. Structures at timestep N have unprimed labels, structures at timestep N+1 have primed labels. The relative sizes of structures are represented with circles of different sizes. Letters above each line represent the type of relation.

The bottom illustration depicts a case where partial splitting occurs. As structure A is larger than structure B, C' is split from A, as rule 3 a) requires. Structure B translates to B', since it is larger than C'. In this situation it appears that C'

is simultaneously split from A and B. To guarantee that this kind of problem can be resolved uniquely, it is chosen that C' is split from the larger structure A, and the smaller structure B contributes with a partial split, having a small part of it split and merge into C'. In the tracking scheme used in this work, partial splitting is ignored, since it conveys little meaningful information and the structures related by it already have "stronger" relations with other structures.

With the logical rules that have been presented in this section, any number of relations between any number of structures at consecutive timesteps can be resolved uniquely. However, because the result depends only on the relative sizes of the structures, situations where there are multiple structures with identical sizes related to the same structure need to be handled in a consistent manner. Here it is chosen that for structures with identical sizes, prioritization is based on the processing order of the structures instead of their size, in such manner that the first structure processed is the "largest" one.

2.3.2 Tracking evolving structures

Tracking structures over a desired time range requires resolving the relations for all the related structures at consecutive timesteps in that range. The tracking of a structure begins when a relation is found between two non-tracked structures at consecutive timesteps. Each tracked structure is represented with an unique ID and has two lists, one for keeping track of the cells belonging to the structure at each timestep, and one for saving the corresponding times.

When a non-tracked structure is found to translate, it will be assigned a new ID and have the cells and times added into their respective lists. Afterwards, the newly tracked structure is placed into a list containing the currently tracked structures. Updating a tracked translating structure works in the same way, but involves only updating the cell and time lists of the structure, as the structure is already in the

tracked list.

To track merging and splitting structures, each structure is provided with a list for its "children". A child is defined to be a tracked structure that is currently merged into another structure. The children of a structure are the structures that have merged into it. When a structure merges into another structure, it is removed from the list containing currently tracked structures and is put into the child list of the structure it merges into. If the merging structure had not been tracked previously, it is first assigned a new ID and created in a similar way as was done with non-tracked translating structures, but it is then added to the child list.

Then, each structure is provided with a list for its "parent" at each timestep. The parent's ID is saved to the list at each timestep, in the same manner as cells and time. A structure's parent at a given timestep is the structure into which the structure in question is currently merged. If the structure is independent, and not merged into any other structures, it is its own parent. Thus, each row on the parent list contains either the structure's own ID or another structure's ID. For generality, if the parent merges, the new parent for both structures is the one into which the old parent merged into. The key idea here is that when a structure is merged, it will be updated with the same cells as its parent.

With the child and parent structures defined, in the case of a splitting event, the child list of the splitting structure is checked for structures. If it is not empty, the latest addition to the list is removed, and put back into the list of tracked structures. The returned structure becomes again its own parent, as per definition of parent. If the child list is empty, the split structure is created as a copy of the splitting structure, but with a new ID. The new structure will retain the history of the parent up to the splitting event, but will be updated individually in the future. It is important that the child list is not copied, because it could result in duplicate structures. In the tracking scheme used in this work, all structures have

two lists for their children, to separate mergers occurring from the upstream and the downstream.

Figure 2.2 illustrates how parent and child structures are utilized in two example situations. For demonstration purposes, each structure has only one child list in the figure. Example case a) of Figure 2.2 represents a situation, where a tracked structure B briefly merges into another tracked structure A. A and B are both independent tracked structures at timestep N. At timestep N+1, B merges into A and becomes a child of A. Similarly, the parent of B changes from B to A. When A splits into two structures at timestep N+3, the split structure is taken from A's child list, since it contains B. Then B is split off and removed from A's child list. Accordingly the parent of B changes from A back to B.

The parent list of B in this example is (B, A, A, B). By looking at it alongside the list containing the times when B existed (t=N, N+1, N+2, N+3), it can be easily seen when B has been merged. These times can be filtered out, in order to study only times when B has existed as a "physical", independent structure. On the other hand, from the list it can be seen with which structures B has interacted with. If B didn't split from A in this example, it would have been kept in A's child list until A was not tracked anymore. B's parent list (B, A, A,..) would allow to easily first follow B until it merges into A, and then switch to A to see how it evolves after B has merged into it.

Example case b) of Figure 2.2 represents a situation where a structure (D) is split from a larger structure (C), and is further itself split up into two structures (D and E). Initially at timestep N, C is the only tracked structure. As the child list of C is empty, no structures are merged into C. When D splits from C at timestep N+1, it must be created. As explained previously, D is created as a copy of C, given its own ID and own list for children. Similarly E is created as a copy of D. When E splits from D and is created, its list of parents is (C, D, E). From it, the whole

a)

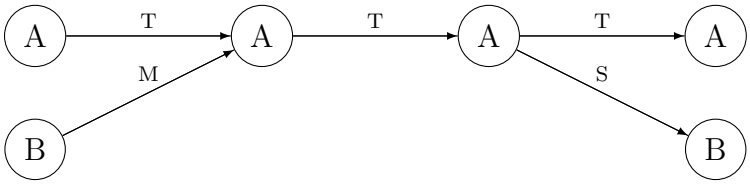

Timestep	N	N+1	N+2	N+3
Parent of A	A	A	A	A
Parent of B	B	A	A	B
Children of A	-	B	B	-
Children of B	-	-	-	-

b)

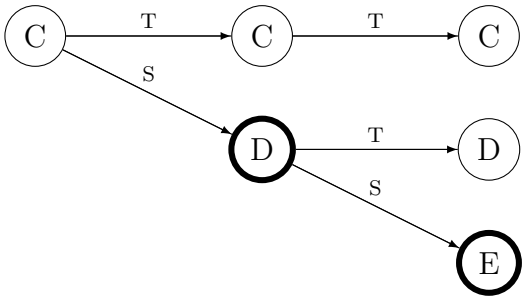

Timestep	N	N+1	N+2
Parent of C	C	C	C
Parent of D	C	D	D
Parent of E	C	D	E
Children of C	-	-	-
Children of D	-	-	-
Children of E	-	-	-

Figure 2.2: Illustrations depicting how parent and child structures work in the tracking scheme developed for this work. Different structures have IDs labeled with letters A,B,C,D,E. Letters T,M,S represents relations as they were defined in section 2.3.1. The structures are aligned with the tables found below them, which show the corresponding timesteps and the parents and the children of the structures at those timesteps. Structures that are created in the middle of tracking are highlighted in bold.

history leading up to the formation of E can be seen.

The tracking of a structure terminates when no more relations are found for it. To account for weak/momentarily disappearing structures, a fixed time limit is used to keep disappeared structures in the tracked structure list for a couple of timesteps. If no new relations are found within the time limit, then the structure is removed from the list of tracked structures and is moved into a list containing disappeared structures.

In the end, each tracked structure has a history showing all the events it has gone through. The cell list shows which cells belong to the structure at each timestep, the time list the corresponding times. The parent list shows the parent of the structure at each timestep. From the parent list, merging events can be retrieved by finding the rows where the parent of a structure changes from itself into another structure. Conversely, the splitting events can be found by finding the rows where the parent changes from another structure to the structure itself.

The practical implementation of this tracking scheme involves some technical details. These are further described in Appendix A, where a pseudocode implementation can be also found.

2.4 Categorization of data

A flexible way to categorize tracked structures is to assign to each structure an n-bit number, where each bit represents some property that the structure can have. This way, a large number of arbitrary categorizations can be made by combining different independent properties, such as "is formed by splitting" and "is formed as an SHFA". The state of each property can be checked by performing a logical AND operation with the bit of the property.

In this work, each structure is represented with a 9-bit number. The bits correspond to the following properties:

Bit	**Property**
0	Exists as a caviton during its lifetime
1	Exists as an SHFA during its lifetime
2	Is formed independently [0] / Is formed via splitting [1]
3	Found at the first timestep of the tracking interval
4	Disappears independently [0] / Disappears via merging [1]
5	Has child structures during its lifetime
6	Is a child structure during its lifetime
7	Type at formation, Caviton [0] / SHFA [1]
8	Type at disappearance, Caviton [0] / SHFA[1]

Bit no. 3 is included in order to be able to identify, and possibly exclude from certain statistics, all cavitons/SHFAs already existing at the very beginning of the tracking interval. For them, it is not possible to tell whether the structures actually formed at that time or had formed before the tracking started.

3. Results

3.1 The simulation run and the output of the tracking

In this work, cavitons and SHFAs were tracked in a single Vlasiator simulation run, which represents the near-Earth space in a 2D-cut in the noon-midnight meridional plane, having Earth at the origin, the x-axis oriented towards Sun and the z-axis pointing northward of the ecliptic and along the Earth dipole. The state of the simulation is available at 0.5 second intervals. A snapshot of the simulation run can be seen in Chapter 1 in Figure 1.7. In the run, the solar wind flows with a velocity of -750 km/s along the x-axis. Protons are the only ion species present in the run, and their density is set to 1 cm^{-3} in the solar wind. The solar wind proton temperature is set to 0.5 MK. The strength of the IMF is set to 5 nT, and its direction is southwards and sunwards at a 45° angle from the x-axis. These solar wind parameters correspond to an Alfvén Mach number of 6.9, a magnetosonic Mach number of 5.6 and β of 0.7.

Cavitons and SHFAs were identified with the density and magnetic field criteria (80% of solar wind values, for SHFAs β>10 in >60% of cells additionally). The minimum size of tracked structures was set to 5 cells, corresponding roughly to an area of 0.011 $R_E{}^2$. The amount of area overlap required for detection of an evolving structure was set to 25%. Disappeared structures were monitored for 5 seconds (10

timesteps), after which they were declared truly disappeared.

The tracking started at 900.0 seconds into the simulation when the bow shock appears well formed. The tracking was carried out until the end of the simulation at 1437.5 seconds. Thus, the total duration of the tracking was 537.5 seconds (1075 timesteps). The number of structures seen at a single timestep of the tracking interval varies between 29 and 72, with the average count being 52. On average, 74.9% of structures seen at a single timestep are cavitons. The percentage of cavitons varies between 56.8%-88.6%. The total amount of structures gathered from all timesteps over the tracking interval is 55,409. Based on this set, 1445 unique structures were detected and tracked. 135 of the 55,409 (0.24%) single timestep structures were not detected to belong to any tracked structures. Of the tracked structures, 1312 (90.8%) formed independently, and the rest 133 (9.2%) formed by splitting from existing structures. 40 of the independently formed structures were detected between the first two timesteps, meaning that they could have formed before the start of the tracking interval. These structures are omitted from statistics concerning formation, lifetime and propagation distance.

The tracked structures were divided into three categories based on their classification as cavitons and SHFAs. The first category is "pure cavitons", which never fulfill the SHFA criterion during their lifetimes. These cavitons thus form as cavitons and do not evolve into SHFAs. The second category is "pure SHFAs", which always fulfill the SHFA criterion. This means they are formed as SHFAs and have not evolved from cavitons. The third category is "cavitons/SHFAs", which include the tracked structures that do not fit into the "pure" categories. This means that they change their classification between a caviton and an SHFA during their lifetime. Of the 1445 tracked structures, 730 (50.5%) structures were classified as pure cavitons, 339 (23.5%) as pure SHFAs and 376 (26%) as cavitons/SHFAs.

The rest of this chapter is structured as follows. The next section details the

formation region of cavitons and SHFAs. Section 3.3 presents statistics about the transients' physical properties. Finally, the topic of section 3.4 is cavitons' and SHFAs' propagation and evolution.

3.2 Formation of cavitons and SHFAs

Structures form evenly in the tracking interval, and there are no significant periods of increased or decreased formation. This was verified by taking a 50-second moving average of the number of forming structures per timestep. The average varies between 0.85-1.4 structures/timestep. There is a slightly increasing trend towards the end, with the average initially fluctuating around 1.0 and in the end around 1.1.

The formation locations of the structures are quantified by using their distance to the bow shock along the IMF (at a 45° angle), and the "nose angle", which is the angle from the Sun-Earth line in respect to Earth at the origin (0° points sunwards along the positive x-axis). A structure's distance to the bow shock is found by following a line from the structure's cell with the smallest x-value at a 45° angle northward, antisunward, to the first cell where the solar wind core temperature is at least four times larger than the ambient solar wind core temperature. This condition is used for the identification of the bow shock crossing. A similar condition was used by Battarbee et al. (manuscript submitted to ANGEO, 2019) [2]. The method for resolving the jump in the solar wind core temperature from spacecraft data is also detailed in Wilson et al. (2014a) [57].

Cumulative histograms of structure formation positions along the IMF direction are shown in Figures 3.1-3.3 for all structures, cavitons and SHFAs, respectively. The categorization of the structures is based on their type at the time of formation. The histograms show only the positions of "naturally" forming structures, and do not include the ones that formed by splitting, or those that "formed" between the first two timesteps of the tracking interval. There are 6 cavitons that formed at the

bottom left corner of the simulation box before the bow shock spanned the whole z-axis. For these, the distance to the bow shock along the IMF could not been calculated, and they are omitted from the data.

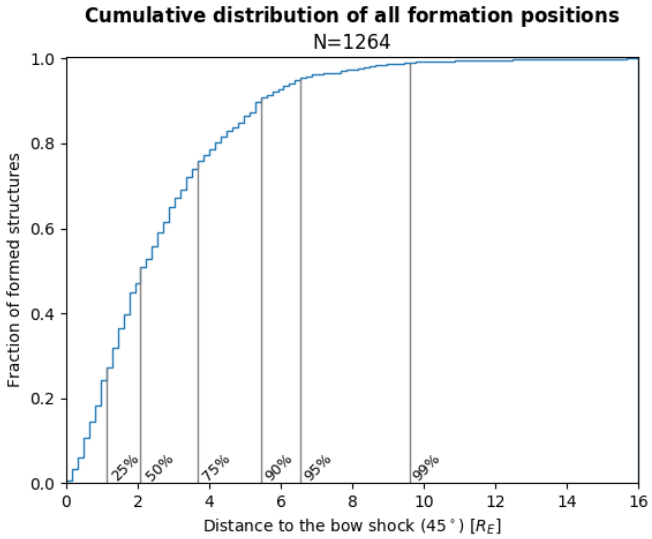

Figure 3.1: Cumulative histogram of all structures' formation positions. Two caviton outliers located at 21.41 R_E and 39.52 R_E are not included in the data.

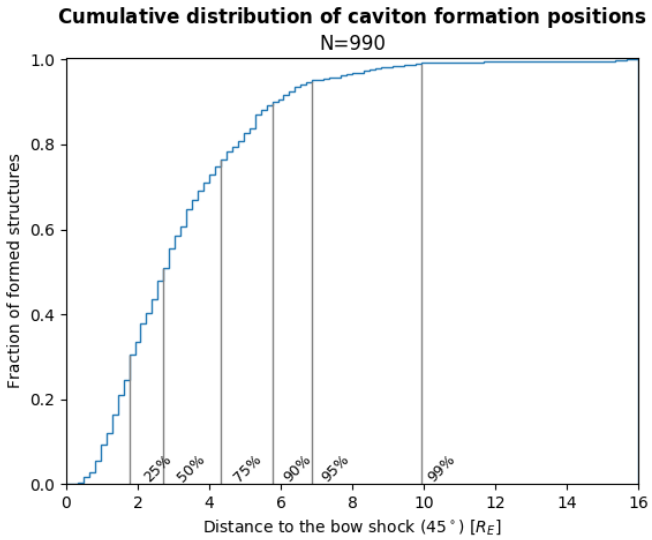

Figure 3.2: Cumulative histogram of cavitons' formation positions. Two outliers located at 21.41 R_E and 39.52 R_E are not included in the data.

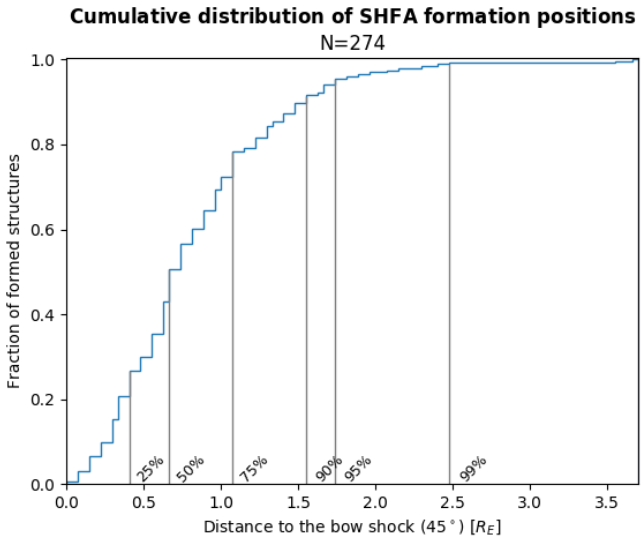

Figure 3.3: Cumulative histogram of SHFAs' formation positions. Note that the x-axis scale is different than in Figures 3.1 and 3.2.

Figure 3.1 shows that 99% of all tracked structures formed within ∼10 R_E from the bow shock. The formation rate appears constant up to 4 R_E from the bow shock, which contains 75% of the formation. Up to 6.5 R_E the formation is still fairly abundant, but beyond this distance structures form scarcely.

The distribution of cavitons' formation positions in Figure 3.2 strongly resembles the distribution containing all structures, as the majority of the forming structures are cavitons. The only noticeable difference is that caviton formation does not start immediately at the bow shock. The caviton closest to the bow shock edge formed at 0.3 R_E. SHFA formation starts at the bow shock, but takes place in a much more restricted region compared to cavitons, as Figure 3.3 shows. Virtually all SHFAs form within 2.5 R_E from the bow shock. SHFA formation is uniform up to ∼1 R_E from the shock, then decreases slightly and continues with a decreased rate until 1.75 R_E. Beyond 1.75 R_E SHFA formation is scarce. Two clear outliers can be seen at ∼3.5 R_E.

More SHFAs than cavitons form within 1.76 R_E from the bow shock (not shown). Within this distance, 501 structures formed in total, of which 243 (48.5%)

were cavitons and 258 (51.5%) were SHFAs. After this point, the number of formed cavitons exceeds the number of formed SHFAs and the SHFA formation rate starts declining as seen in Figure 3.3. In the SHFA formation region ($\lesssim$ 2.5 R_E), 432 cavitons formed in total, compared to 272 SHFAs. Closer than 0.3 R_E to the bow shock where no cavitons formed, 27 SHFAs formed in total.

Figure 3.4 shows the formation positions of cavitons and SHFAs as 2D heatmaps. The formation rate is shown in two different coordinate systems. The left panels of Figure 3.4 show the rate in the Cartesian space using the GSE-coordinate system, where Earth is at the origin, the x-axis is the Earth-Sun line and the z-axis points northward of the ecliptic. Because the bow shock experiences some sunward expansion during the simulation run, the Cartesian plots are supplemented with plots in the distance to the bow shock (along the IMF) vs. the nose angle coordinate system, which are shown in the right panels. In this coordinate system, the expansion of the bow shock is accounted for as the distance to the bow shock is used instead of absolute position in the GSE coordinates. The expansion of the bow shock occurs due to 2D effects, as a result of magnetic field piling up in front of the magnetosphere. In the left panels, every pixel has dimensions of 2×2 $R_E{}^2$ and in the right panels, each pixel has a height of 5° and a width of 0.5 R_E.

On the top row of Figure 3.4, the formation rate is shown for all structures. In the top right panel, it is seen that the formation region greatly expands away from the bow shock. As the movement of the shock is taken into account in the coordinate system used in this panel, the expansion is independent of the movement. Near the bow shock nose, the size of the formation region is limited by the foreshock edge between nose angles −20° and −50°. At its largest, the uniform structure formation extends up to 10 R_E from the bow shock, at nose angles −90° to −110°. After this, the widening of the formation region stops and the formation stops completely at −130°, as the nose angle reaches the corner of the simulation box.

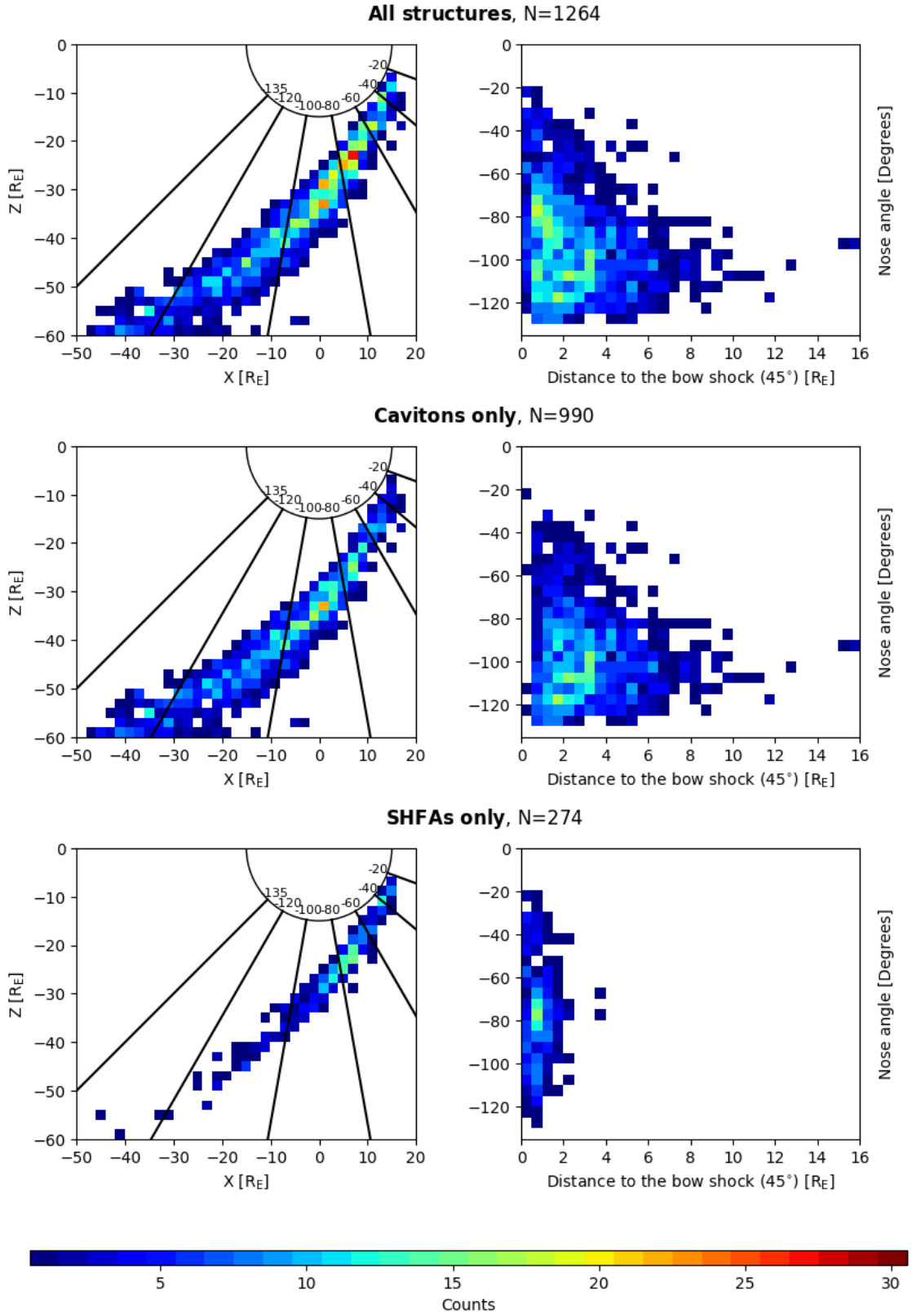

Figure 3.4: Heatmaps of structure formation for all structures (top row), cavitons (middle row), and SHFAs (bottom row). The left column shows the formation in the Cartesian space using GSE-coordinates, and the right column in the distance to the bow shock vs. nose angle coordinate system. Left panels contain an overlay showing the nose angle for easier comparison.

It is possible that the formation region could continue extending at nose angles larger than $-110°$, if not limited by the simulation box. In the Vlasiator study of Blanco-Cano et al. (2018) [4], using the same simulation run as this work, it was demonstrated that cavitons and SHFAs form along "fingers" of abundant particle reflection. The length of these fingers increases with nose angle until they are cut off by the lower boundary of the simulation box. The cut-off occurs at a nose angle of $\sim -100°$ at the first timestep of the tracking interval and at $\sim -95°$ at the last timestep of the interval. These angle coincide with the area where the formation region extends the furthest and starts shrinking.

Comparing the panels on the top row of Figure 3.4, it seems that the regions where the formation rate peaks differ in location in the different coordinate systems. Based on the examination of the top-left panel, the formation rate appears to peak between nose angles $-60°$ and $-90°$ and decrease slightly towards larger nose angles. In the top-right panel, the increased formation rate appears to continue to nose angles beyond $-90°$. This could be partially an effect of the nose angle coordinate system's geometry. A larger portion of the formation region is sampled at larger nose angles, as the nose angle direction differs significantly from the bow shock normal at high latitudes. The effect is most significant at a nose angle of $\sim -110°$, as seen in the top-left panel of Figure 3.4. Regardless, it can be inferred from the plots that the formation is most signficant near the bow shock at distances of $\sim$0.5-4 R_E for all nose angles. Interestingly, the formation rate drops sharply at $<$0.5 R_E from the bow shock.

The middle and the bottom rows of Figure 3.4 show the 2D formation heatmaps for cavitons and SHFAs separately. Compared to the top row, the formation rate in the caviton heatmaps appears to be slightly reduced at nose angle $\sim -80°$. A notable feature in the right panel of the middle row is the very low caviton formation rate at $<$0.5 R_E, which explains the drop in the heatmap for all structures. For SHFAs, it is

easy to see that the formation rate peaks at $\sim -80°$ and decreases towards large nose angles. Far away from the bow shock nose very few SHFAs form, whereas caviton formation is abundant.

3.3 Physical properties of cavitons and SHFAs

3.3.1 Global properties

Statistics about the physical properties of cavitons and SHFAs, including number densities, magnetic field strengths, temperatures, β, bulk flow speeds and areas are shown in Tables 3.1-3.4. The same classification of tracked structures is used as introduced in Section 3.1. The quantities shown are calculated as extrema over the lifetime of each tracked structure, such as overall minimum number density measured over a structure's lifetime. A structure's "lifetime" starts at its formation and ends at its disappearance. The times when structures are momentarily merged into other structures are ignored. The columns in the tables show the minimum, maximum, average and median of the data gathered from all structures in the class.

The statistics calculated for all structures are shown in Table 3.1. The minimum values of total number density n and magnetic field magnitude $|B|$ show decreases of 20.2-73.5% and 20.1-94.0% from the ambient solar wind values, respectively. On average, the depressions are 31.4% and 32.32% from solar wind values. The minimum core number density n_{core} and the maximum suprathermal number density $n_{st.}$ show large variation, ranging from the 80% caviton criterion limit to densities of $<10^{-2}$ cm^{-3}. Here, core refers to the population making up the solar wind, and suprathermal to the population outside it, containing the backstreaming protons. The overall minimum core density is notably lower than the overall minimum number density, implying that the core can get very depleted and be replaced with suprathermals. The overall maximum value of suprathermal number density

shows an example where a part of a structure is filled with suprathermals up to the caviton criterion limit of $0.8n_{sw}$. The proton temperature T has values reaching from near the solar wind value (0.5 MK) up to 100 times the solar wind value. All temperatures above 30 MK occurred within ∼0.5 R_E from the shock. Similarly, β values above 100 occurred within ∼0.6 R_E from the shock. The overall highest β was caused by a small part of structure partially crossing into the bow shock. The bulk flow speed $|v_{flow}|$ mostly appears slower than the solar wind. On average, the bulk flow speed is reduced by ∼91 km/s or 12.1% from the solar wind flow speed (750 km/s) and the largest reduction is ∼495 km/s or 66.0%. For 60 structures, the minimum speed is above the solar wind flow speed. The areas of the structures range from the 5 cell limit (0.011 R_E^2) up to ∼1.9 R_E^2. Most of the structures are small (of the order of 0.1 R_E^2), as seen from the small average and median.

All structures, N=1445				
Quantity	**Min.**	**Max.**	**Average**	**Median**
Min. n [cm^{-3}]	0.265	0.798	0.686	0.712
Min. n_{core} [cm^{-3}]	0.011	0.797	0.610	0.650
Max. $n_{st.}$ [cm^{-3}]	2E-4	0.778	0.122	0.073
Min. $\|B\|$ [nT]	0.299	3.996	3.384	3.568
Max. T [MK]	0.668	50.522	7.811	6.012
Max. β	1.2	4305.2	27.7	11.6
Min. $\|v_{flow}\|$ [km/s]	255.3	783.5	658.9	683.6
Max. A [R_E^2]	0.011	1.909	0.145	0.073

Table 3.1: Statistics of physical properties calculated for all tracked structures. The quantities shown are the extrema over the tracked structures lifetime. From top to bottom: Total proton number density n, core proton number density n_{core}, suprathermal proton number density $n_{st.}$, magnetic field strength $|B|$, proton temperature T, plasma β, bulk flow speed $|v_{flow}|$ and structure area A.

Pure cavitons, N=730				
Quantity	**Min.**	**Max.**	**Average**	**Median**
Min. n [cm^{-3}]	0.481	0.798	0.732	0.746
Min. n_{core} [cm^{-3}]	0.433	0.797	0.702	0.715
Max. $n_{st.}$ [cm^{-3}]	2E-4	0.186	0.038	0.032
Min. $\|B\|$ [nT]	2.224	3.996	3.677	3.758
Max. T [MK]	0.668	9.801	3.526	3.373
Max. β	1.2	26.8	6.6	6.2
Min. $\|v_{flow}\|$ [km/s]	519.7	773.7	707.7	713.1
Max. A [R$_E{}^2$]	0.011	1.410	0.114	0.062

Table 3.2: Statistics of physical properties calculated for pure cavitons only. See Table 3.1 for explanation.

Pure SHFAs, N=339				
Quantity	**Min.**	**Max.**	**Average**	**Median**
Min. n [cm^{-3}]	0.298	0.796	0.664	0.681
Min. n_{core} [cm^{-3}]	0.011	0.763	0.506	0.541
Max. $n_{st.}$ [cm^{-3}]	0.035	0.778	0.230	0.185
Min. $\|B\|$ [nT]	0.458	3.949	3.171	3.349
Max. T [MK]	4.026	50.522	13.658	12.007
Max. β	10.5	1036.0	45.3	27.9
Min. $\|v_{flow}\|$ [km/s]	255.3	766.5	599.8	612.9
Max. A [R$_E{}^2$]	0.011	0.687	0.076	0.040

Table 3.3: Statistics of physical properties calculated for pure SHFAs only. See Table 3.1 for explanation.

Cavitons/SHFAs, N=376				
Quantity	**Min.**	**Max.**	**Average**	**Median**
Min. n [cm^{-3}]	0.265	0.795	0.616	0.639
Min. n_{core} [cm^{-3}]	0.094	0.762	0.527	0.562
Max. $n_{st.}$ [cm^{-3}]	0.035	0.649	0.188	0.151
Min. $\|B\|$ [nT]	0.299	3.968	3.006	3.149
Max. T [MK]	5.079	39.957	10.859	9.810
Max. β	10.2	4305.2	52.9	21.3
Min. $\|v_{flow}\|$ [km/s]	299.8	783.5	617.6	629.5
Max. A [R$_E{}^2$]	0.011	1.909	0.269	0.171

Table 3.4: Statistics of physical properties calculated for cavitons/SHFAs only. See Table 3.1 for explanation.

Comparison between Table 3.2 and Table 3.3 shows how "pure" cavitons and SHFAs differ from each other. On average, the density and magnetic field depressions are deeper inside SHFAs than cavitons. For cavitons, the density and magnetic field have 26.8% and 26.5% decreases from the ambient solar wind values. For SHFAs, the same numbers are 33.6% and 36.6%. The total number density decreases appear greater inside SHFAs, despite them having significantly more suprathermals inside them. The average suprathermal density inside cavitons is very low (0.038 cm^{-3}), and the maximum is lower than the average inside SHFAs (0.186 cm^{-3} vs. 0.230 cm^{-3}). The suprathermal density inside SHFAs can rise close to the caviton criterion limit as seen by the maximum. The proton temperature is much greater inside SHFAs than cavitons, and it is clear that it is the cause of the increased β inside SHFAs. The average bulk flow speed is close to the solar wind flow speed inside cavitons ($\sim$42 km/s or 5.6% reduction) and more reduced inside SHFAs ($\sim$150 km/s or 20.0% reduction). The overall minimum bulk flow speed inside SHFAs

(255.3 km/s) is also significantly lower than inside cavitons (519.7 km/s). The sizes of cavitons are on average larger than those of SHFAs ($\sim$0.11 R_E^2 vs. $\sim$0.08 R_E^2). The largest caviton is over twice as large as the largest SHFA. The median sizes are similar, showing that majority of both cavitons and SHFAs are small.

Table 3.4 shows "cavitons/SHFAs", the structures that change classification between a caviton and an SHFA during their lifetime. They exhibit the overall smallest values of total number density and magnetic field strength, which are on average reduced from the solar wind values by 38.4% and 39.9%, respectively. The larger depressions of density inside cavitons/SHFAs compared to pure SHFAs appear to be due to slightly lower suprathermal densities. The other properties associated with SHFAs (core depletion, heating and bulk flow speed reduction) also appear slightly weaker inside cavitons/SHFAs than pure SHFAs. They are however notably stronger than inside pure cavitons. The structures in the cavitons/SHFAs-category are the largest overall, over twice as large as pure cavitons on average ($\sim$0.27 R_E^2 vs. $\sim$0.11 R_E^2). At the time when they reach their maximum area, 214 caviton/SHFA-structures were classified as cavitons and 162 as SHFAs.

3.3.2 Distributions of the physical properties

Figure 3.5 shows the distributions of the quantities shown in Tables 3.1-3.4, excluding the core number density and β. The core number density is excluded because its distribution closely resembles the total number density, and the distribution of β is excluded as the same information is observable from the distribution of the temperature. In the panels of Figure 3.5, the structures are simply classified into cavitons and SHFAs depending on their type at the time of the quantities' extrema. The distributions of the proton temperature and the area contain some outliers, which have been excluded. In total, there are 11 structures with T=31.13-50.52 MK and 16 structures with A=1.02-1.91 R_E^2.

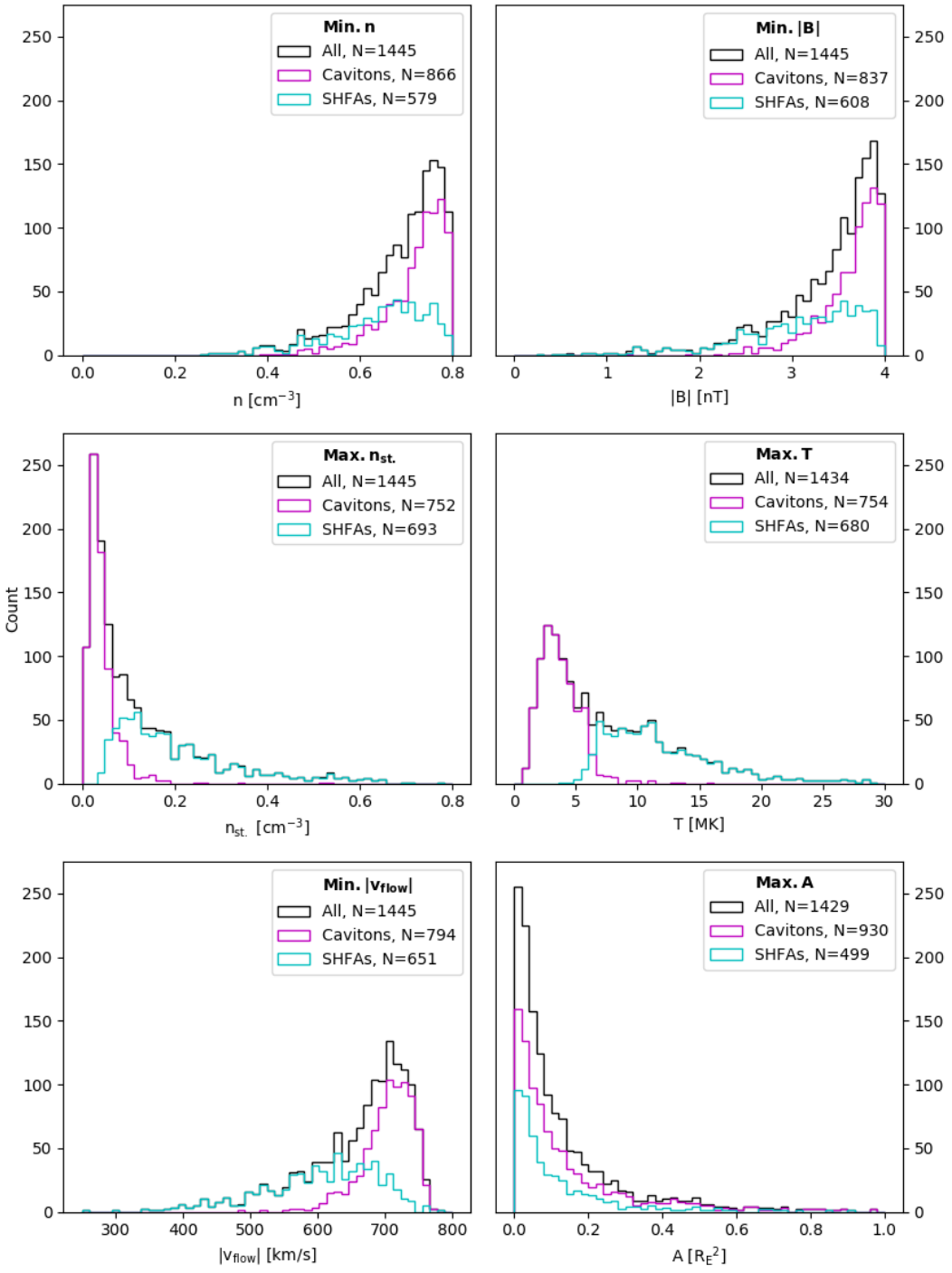

Figure 3.5: Distributions of different physical properties of cavitons and SHFAs. Like in Tables 3.1-3.4, the quantities are the extrema over the tracked structures lifetime. The types of the structures are the types during the times of the quantities' extrema. From left to right, top to bottom: Min. total proton number density n, min. magnetic field strength $|B|$, max. suprathermal proton number density $n_{st.}$, max. proton temperature T, min. bulk flow speed $|v_{flow}|$ and max. structure area A. Outliers have been omitted from the distributions of T and A.

The distributions of the total number density n and magnetic field strength $|B|$ appear similar. The only slight difference is that there are some very large depressions in the magnetic field that are not present in the density. Cavitons appear peaked near the 80% caviton criteria, and do not appear to generally have depressions larger than 60% from the solar wind values. SHFAs are more spread at different levels of depressions than cavitons, and are more numerous at large depressions. The distribution of the core number density (not shown) appears similar to the distributions of n and $|B|$, but has the SHFA distribution slightly shifted towards low values, extending to $\lesssim$0.2 cm^{-3}.

The distribution of the suprathermal number density $n_{st.}$ is highly peaked for cavitons at low values, slightly below the start of the SHFA distribution at $\sim$0.05 cm^{-3}. The overlapping region between the cavitons and SHFAs is small, as the cavitons extend only to 0.2 cm^{-3} with the exception of 5 outliers. The SHFA distribution extends well above 0.6 cm^{-3}. To check that the high suprathermal densities inside SHFAs are not due to single cells, the same distribution but with the maximum average suprathermal density was plotted (not shown), and was found to be almost identical. The proton temperature T shows a clear cut-off between cavitons and SHFAs roughly at $\sim$7 MK. It must be however noted that the temperature is directly proportional to β, which was used as the criterion to distinguish SHFAs from cavitons.

The distribution of the bulk flow speed $|v_{flow}|$ shows that cavitons peak slightly below the solar wind flow speed, in the 650-750 km/s range. Speeds of less than 600 km/s are rare for cavitons. Below this limit, almost all structures are SHFAs. The distribution of SHFAs is clearly shifted away from the solar wind flow speed, and some speeds lower than $\lesssim$400 km/s can be seen. It is worthwhile to note here that the reduction in bulk flow speed does not necessarily signify a slowdown of the solar wind flow. Since the bulk flow speed is computed from the first velocity moment of

the velocity distribution function, two counterstreaming ion populations result in a reduced bulk flow speed (Parks et al., 2017) [34]. It is reasonable to assume that the dramatic slowdowns observed here are due to the accumulation of backstreaming suprathermal ions inside the structures.

The areas of cavitons and SHFAs appear to have similar distributions. As was seen in Table 3.3, "pure" SHFAs only reached a maximum size of $\sim$0.69 R_E^2. Including the outliers between 1-2 R_E^2, there are 7 SHFAs in the "cavitons/SHFAs"-category above this value. In the cavitons/SHFAs-category, 214 (56.9%) structures attained their maximum area as cavitons and 162 (43.1%) as SHFAs, showing that the area maximum can either occur as a caviton or an SHFA.

3.3.3 Correlations between the physical properties

The quantities studied in the preceding sections were tested for possible correlations. Figures 3.6-3.8 show the most relevant and interesting ones. The values were chosen such, that the extreme value over lifetime is used for the quantity on the x-axis, and the extreme value from the same timestep is used for the quantity on the y-axis. After this, the Pearson correlation coefficient was calculated for these quantities for all structures, cavitons only and SHFAs only.

Figure 3.6 shows the correlation between the overall minimum total number density n and the minimum magnetic field strength $|B|$ at the same timestep. Cavitons show a good correlation ($C = 0.793$), whereas SHFAs have notably more spread ($C = 0.575$). The effect of suprathermal ions can be seen by replacing the total number density with the core number density (not shown). In that case, the correlation for cavitons stays roughly the same ($C = 0.79$) and the correlation coefficient for SHFAs climbs to $C = 0.695$. Most of the SHFA scatterpoints in the $\sim$0.5-0.8 cm^{-3} range below the caviton scatterpoints disappear, improving the correlation.

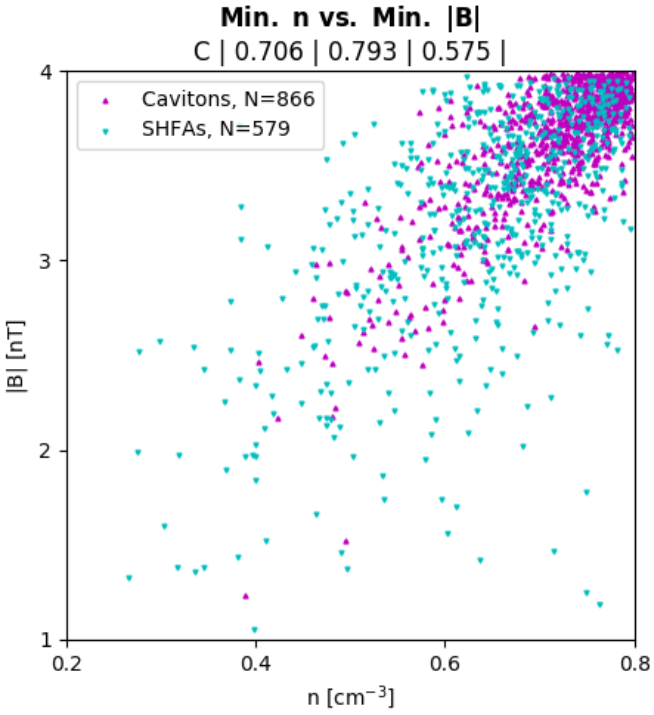

Figure 3.6: Scatterplot of the minimum total number density n over lifetime against the minimum magnetic field strength $|B|$ at the time of the density minimum. The classification of the structures is based on the type during the density minimum. The values labelled 'C' show the Pearson correlation coefficient for all structures, cavitons and SHFAs, respectively.

In Figure 3.7, the correlation between the overall maximum suprathermal number density $n_{st.}$ and the maximum temperature T from the same timestep is shown. The temperature clearly rises inside cavitons with the increasing suprathermal density ($C = 0.782$). Overall good correlation can be seen up to $\sim$0.3 cm^{-3}, after which the points become spread. In Figure 3.5 temperatures above 30 MK were not shown. Here it is seen that the temperature rarely exceeds this value, even with large amounts of suprathermals. As a check, a scatterplot with the maxima replaced by maxima of average values was made (not shown). The plot appears similar, with slightly worse correlation coefficients C| 0.79 | 0.768 | 0.609 |.

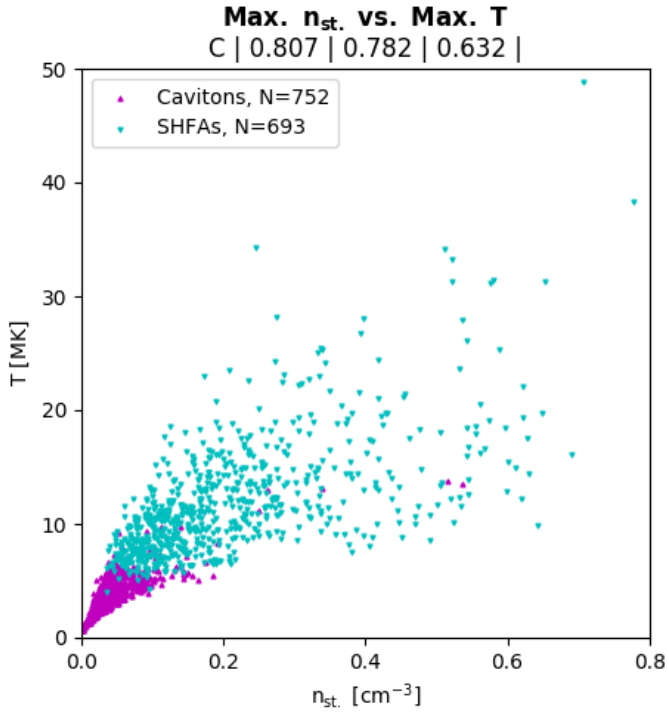

Figure 3.7: Scatterplot of the maximum total number density $n_{st.}$ over lifetime against the maximum proton temperature T at the time of the density maximum. The classification of the structures is based on the type during the density maximum. The values labelled 'C' show the Pearson correlation coefficient for all structures, cavitons and SHFAs, respectively.

Figure 3.8 shows the correlation between the minimum bulk flow speed $|v_{flow}|$ and the maximum suprathermal number density $n_{st.}$ from the same timestep. Now the correlation is stronger for SHFAs ($C = -0.711$), showing that the bulk flow speed decreases with increasing suprathermal density. Cavitons show a weaker correlation ($C = -0.609$), and it appears that their bulk flow speeds can decrease to ∼600-650 km/s without significant accumulation of suprathermals.

The structure area and the depressions of the density and the magnetic field were also checked for possible correlations (not shown). The correlation coefficient for the minimum total density and the area at the minimum is -0.702 for cavitons, -0.593 for SHFAs and -0.562 for both types combined. The correlation coefficients for the minimum magnetic field magnitude and the area at the minimum are -0.72,

-0.405

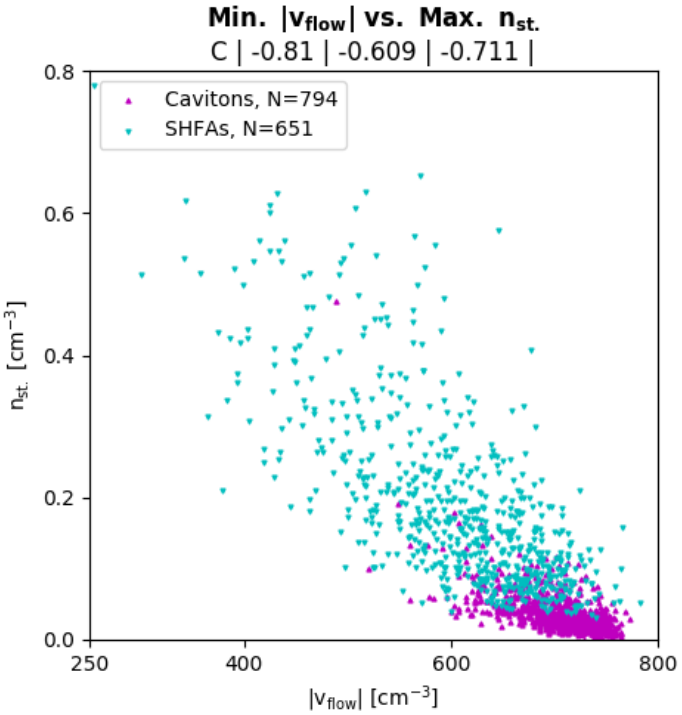

Figure 3.8: Scatterplot of the minimum bulk flow speed $|v_{flow}|$ over lifetime against the maximum total number density $n_{st.}$ at the time of the bulk flow speed minimum. The classification of the structures is based on the type during the bulk flow speed minimum. The values labelled 'C' show the Pearson correlation coefficient for all structures, cavitons and SHFAs, respectively.

and -0.403 for cavitons, SHFAs and both types combined, respectively. The correlation coefficients for cavitons indicate that larger cavitons appear to have larger density and magnetic field depressions. The same is not seen for SHFAs, which could be due to SHFAs shrinking as their suprathermal density increases. With large enough quantities of suprathermals, the total density in the outer parts of an SHFA can increase above the caviton limit ($0.8n_{sw}$) and the structure will decrease in size.

3.3.4 Physical properties' dependence on the position relative to the bow shock

The dependence of cavitons' and SHFAs' physical properties on the bow shock distance and the nose angle were studied with box-and-whiskers-plots, showing how the properties vary with location. Figures 3.9 and 3.10 show the variation as a function of the distance from the bow shock (along the IMF direction) for cavitons and SHFAs, respectively. Similar plots but as a function of the nose angle are shown in Figures 3.11 and 3.12. As before, the shown quantities are extrema over the structures' lifetime. The boxes contain the data in the interquartile range, and the whiskers extend to the 1st (lower whisker) and 99th (upper whisker) percentiles. Outliers are shown with crosses. Figures 3.9 and 3.10 have been cut out at 12 R_E since there are very few datapoints beyond it.

Looking at Figures 3.9 and 3.10, it is evident that the physical properties of cavitons and SHFAs vary with the distance to the bow shock. The general trend is that the minima deepen towards the bow shock and the maxima increase. The minima of total number density n and magnetic field strength $|B|$ appear generally shallow ($\sim$0.7 cm^{-3}, $\sim$3.5 nT) at distances of $>$5 R_E from the bow shock. The suprathermal densities $n_{st.}$ start increasing only at distances of $<$1 R_E from the shock. There are some high suprathermal densities inside cavitons near the shock, which may correspond to structures near the SHFA-limit. Some SHFAs near the bow shock have very depleted cores and lots of suprathermals, as seen by long whiskers at $<$1 R_E. Proton temperatures T start increasing towards the bow shock at $\sim$4 R_E and mostly stay below 10 MK inside cavitons. At 2 R_E from the shock, cavitons have temperatures of $\sim$5 MK, while the SHFAs' temperatures are notably higher, around $\sim$10 MK. The value range of β clearly rises towards the bow shock (note that the scale is logarithmic). Similar to density and magnetic field depressions, the bulk flow speed $|v_{flow}|$ starts slowing down and shifting away from the solar

wind speed at $\sim$4 R_E. The reduction in bulk flow speed is clearly stronger inside SHFAs than inside cavitons near the bow shock. Structure areas A steadily increase towards the bow shock, but the increase is mostly evident in the whiskers. The interquartile range stays fixed at smallest areas while the whiskers grow, meaning that only the portion of structures in the upper quartile range grow. Again, cavitons appear generally larger than SHFAs.

The variation of physical properties with nose angle is much less prominent than with bow shock distance, as seen in Figures 3.11 and 3.12. For cavitons, no clear trends are seen, with the exception of some slightly deeper magnetic field depressions and larger areas at nose angles between $-120°$ and $-85°$. This coincides with the region where caviton formation is most abundant and extends the furthest. SHFAs exhibit more variation with the nose angle than cavitons. Interestingly, the depressions of the magnetic field are deepest at large nose angles, which is not seen in the density depressions. A clear variation is seen in the temperature, which increases towards the bow shock nose. A corresponding trend is seen in the bulk flow speed, which appears to decrease towards the bow shock nose, most prominently at angles closer than $\sim -40°$ to the nose. The areas of SHFAs do not show similar preference to nose angles between $-120°$ and $-85°$ as cavitons do, suggesting that the larger areas of cavitons in that region are due to their more extended formation region.

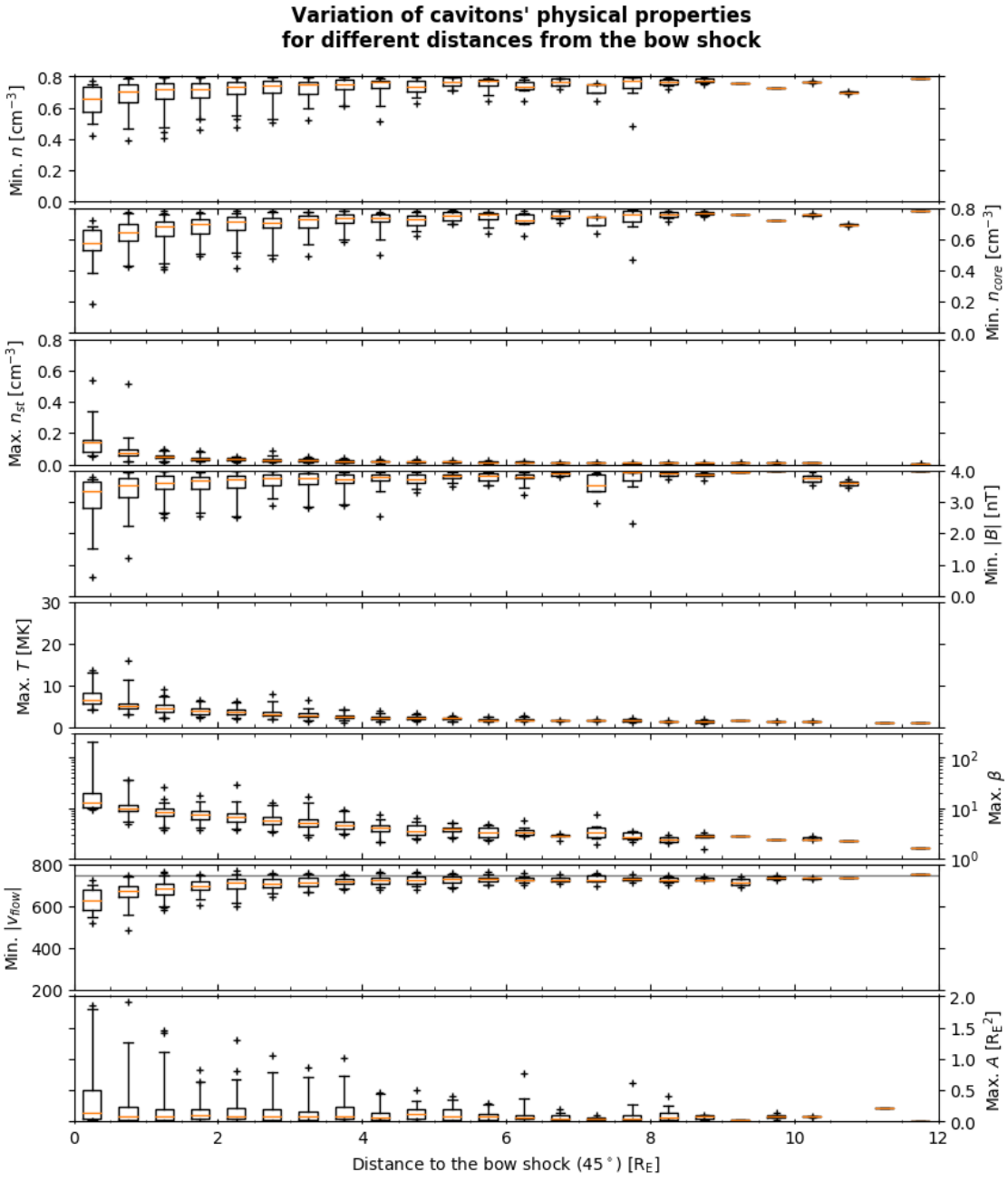

Figure 3.9: A box-and-whiskers plot showing the variation of cavitons' physical properties with the distance to the bow shock, as measured along the IMF direction. The quantities are the same as in Tables 3.1-3.4. Each box covers a distance of 0.5 R_E on the x-axis, data beyond 12 R_E is not shown. The boxes contain the data in the interquartile range, the whiskers extend to the 1st (lower whisker) and 99th (upper whisker) percentiles and outliers are shown with crosses. A grey horizontal line in the $|v_{flow}|$-panel shows the solar wind speed.

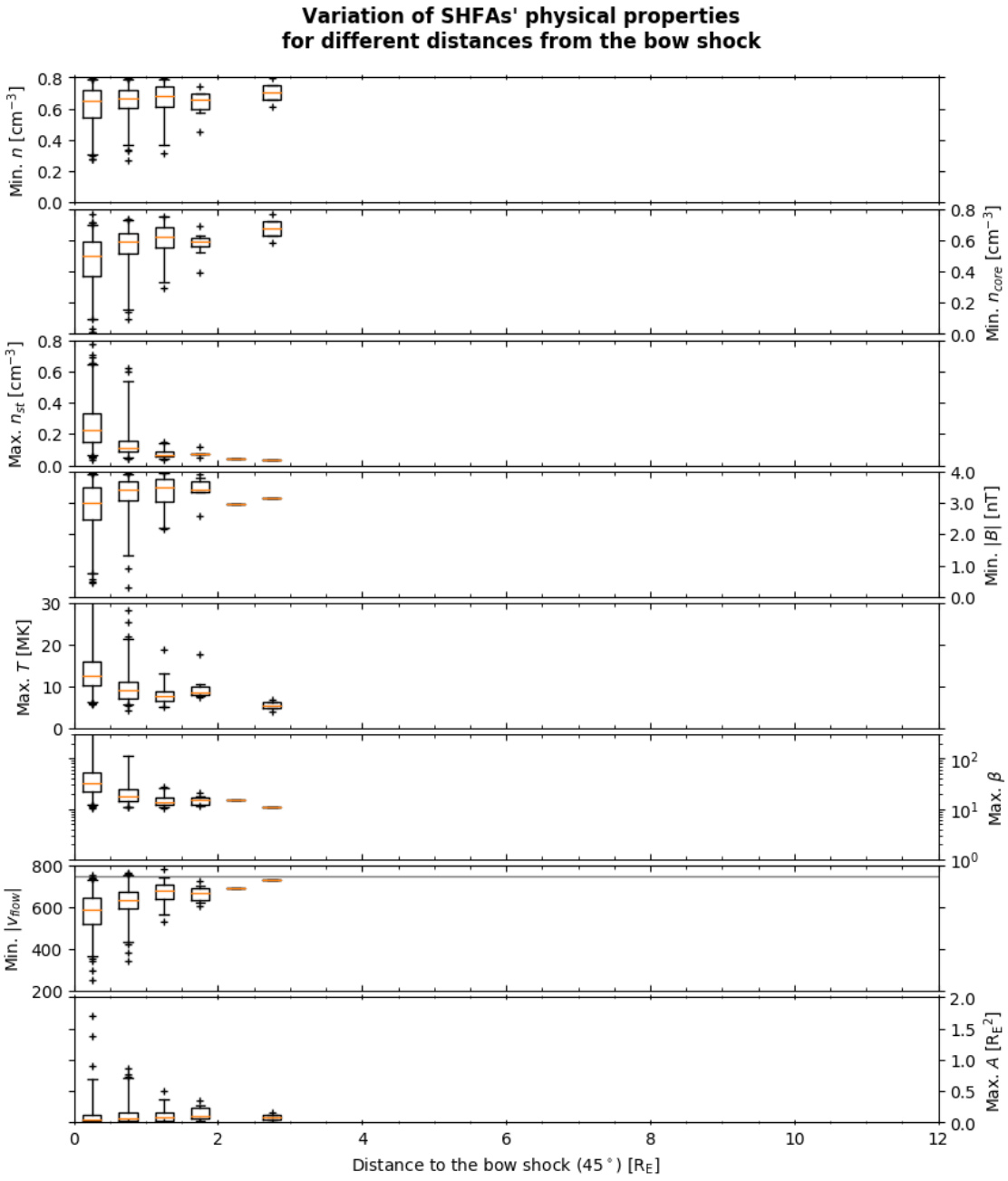

Figure 3.10: A box-and-whiskers plot showing the variation of SHFAs' physical properties with the distance to the bow shock, as measured along the IMF direction. See Figure 3.9 for explanation.

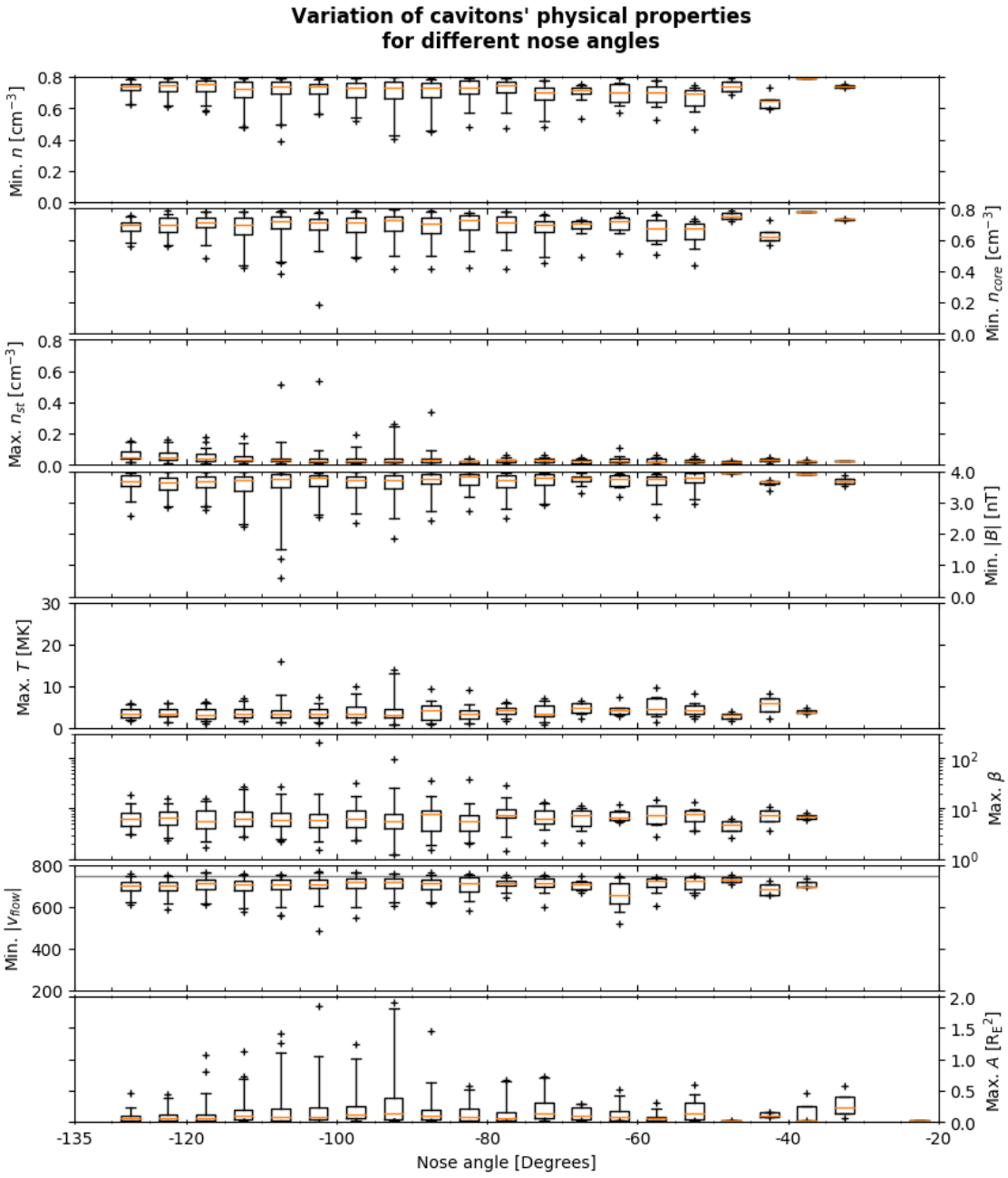

Figure 3.11: A box-and-whiskers plot showing the variation of cavitons' physical properties with the nose angle. The quantities are the same as in Tables 3.1-3.4. Each box covers an angle of 5° on the x-axis. The boxes contain the data in the interquartile range, the whiskers extend to the 1st (lower whisker) and 99th (upper whisker) percentiles and outliers are shown with crosses. A grey horizontal line in the $|v_{flow}|$-panel shows the solar wind speed.

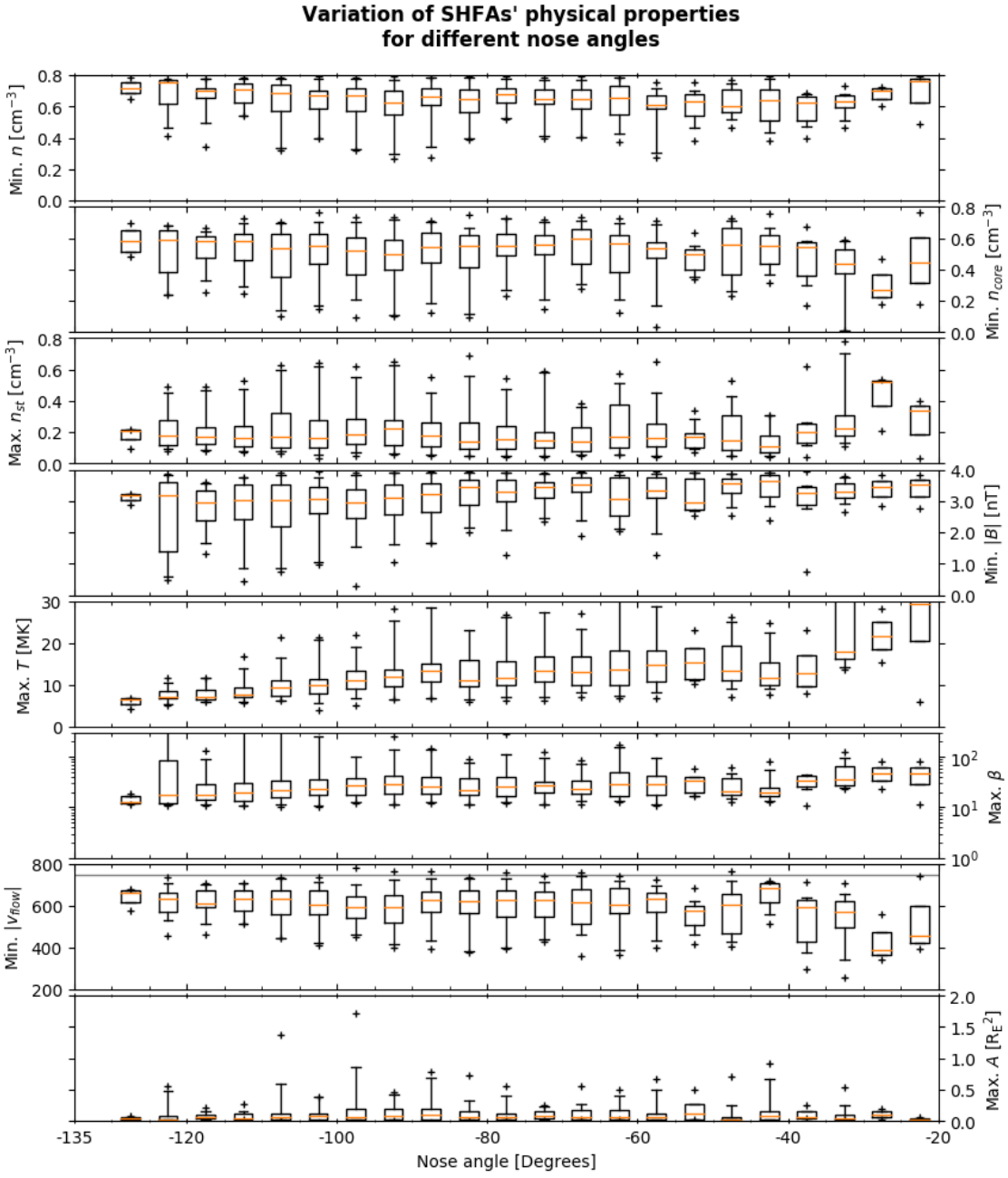

Figure 3.12: A box-and-whiskers plot showing the variation of SHFAs' physical properties with the nose angle. See Figure 3.11 for explanation.

3.4 Propagation and evolution

The lifetimes of the tracked structures are shown in Figure 3.13. As earlier, the lifetime of a structure is defined as the time between its formation and disappearance. The structures shown in Figure 3.13 are classified into "pure" cavitons, "pure" SHFAs and "cavitons/SHFAs" as earlier in this chapter. The plot is cut-out at 120 s, beyond which there are 8 outliers with lifetimes of 126.5-217.0 s.

It is seen that the structures are mostly short-lived, and structures existing for over 60 s are rare. Pure SHFAs are the shortest-lived, which fits the notion of them forming close to the bow shock. Pure cavitons have somewhat similar distribution to pure SHFAs, but they can survive for longer times. Cavitons/SFHAs contain only few very short-lived structures, as they have to exist long enough to transition from a caviton into an SHFA. The longest-lived structures appear to consist of roughly equal numbers of pure cavitons and cavitons/SHFAs.

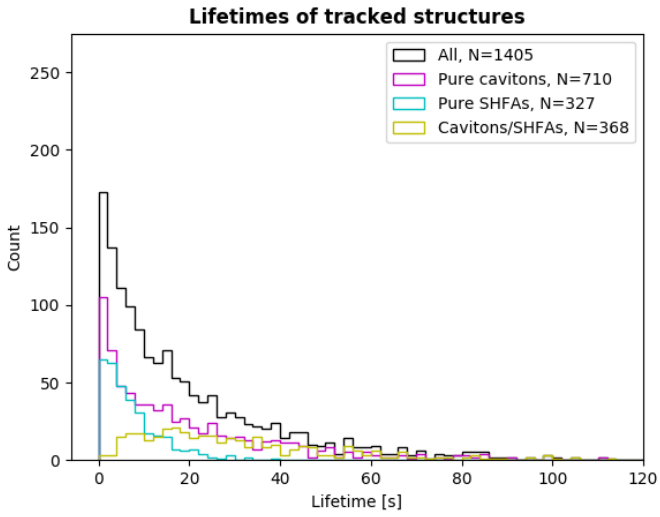

Figure 3.13: The lifetimes of the tracked structures. The lifetime of a structure is defined as the time between the formation and the disappearance of the structure, and can contain brief mergers inbetween. Structures that were found to "form" between the first two timesteps have been ignored. The plot is cut out at 120 s, resulting in 8 outliers.

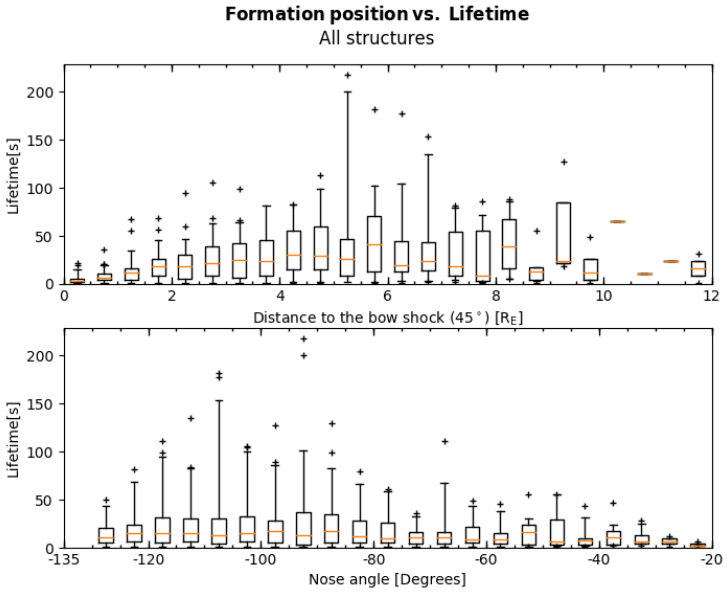

Figure 3.14: Dependence of the structures' lifetimes on formation position. Upper panel: Dependence on the distance to the bow shock (along the IMF). Lower panel: Dependence on the nose angle. The x-axis on the upper panel is cut out at 12 R_E. See Figures 3.9 and 3.11 for details of the box-and-whiskers plots' parameters.

The structures' lifetimes dependence on the formation position is shown in Figure 3.14 as box-and-whiskers plots. The upper panel shows the formation positions' distances from the bow shock along the IMF, and the lower panel the nose angles of the formation positions. As expected, the lifetimes of structures shorten approaching the bow shock, as seen in the upper panel of Figure 3.14. Further away, at distances greater than ∼4-5 R_E from the shock, the interquartile boxes stop growing, but the upper whiskers show some long-lived structures forming at varying distances. Beyond ∼8.5 R_E structure formation starts to decrease, and mostly weak, short-lived structures form. The lower panel shows the dependence on the nose angle. The distribution supports the idea that largest and longest-lived structures form where the formation region extends the furthest away from the bow shock, with the peak between nose angles $-120°$ and $-85°$.

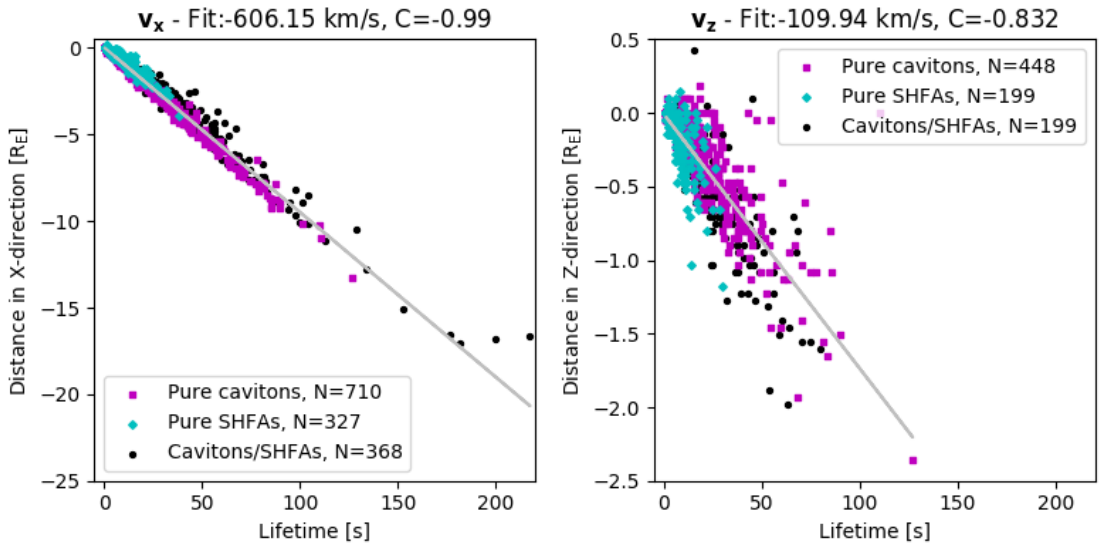

Figure 3.15: Scatterplots of tracked structures' lifetimes vs. propagation distance in the x-direction (left panel) and the z-direction (right panel). A linear fit with correlation C shows the approximate propagation speed in each direction.

Figure 3.15 shows scatterplots of the structures' lifetimes against their travel distances in x and z-directions, which allows to calculate the propagation speed of the structures. In these plots, the positions of the structures are taken as the points where their magnetic field depression is the deepest. The left panel of Figure 3.15 shows the travel distances in the x-direction. The correlation between the structures' lifetime and travel distance is excellent ($C = -0.99$), and a linear fit made from the data shows a propagation speed of $v_x \simeq -606.15$ km/s. As the solar wind moves in the x-direction with a speed of -750 km/s, the x-directional propagation speed in the solar wind rest frame is 143.85 km/s. This shows that cavitons and SHFAs propagate sunward in the solar wind rest frame.

The right panel shows the travel distances in the z-direction. As the distances along the z-axis are very small, they are susceptible to errors from structures' deformation, splitting, merging and other "random" movement of the structure center. To minimize these effects, the plot includes only those structures which do not split/merge from/into other structures. Despite the problems mentioned above, a

linear fit with a good correlation ($C = -0.832$) between the lifetime and the travel distance in the z-direction shows that structures tend to move southwards, away from the bow shock nose with a velocity of $v_z \simeq -109.94$ km/s. The distribution of the pure SHFAs appears somewhat more sloped than that of the pure cavitons and cavitons/SHFAs. Linear fits made separately for the different categories show a z-direction speed of -100.84 km/s for pure cavitons ($C = -0.843$), -155.77 km/s for pure SHFAs ($C = -0.704$), and -132.6 km/s for cavitons/SHFAs ($C = -0.841$).

The evolution of cavitons into SHFAs can be studied by looking at the structures in the "cavitons/SFHAs"-category, which includes the structures that change their classification between a caviton and an SHFA. In total, there are 376 structures in this category, majority of which (338) are born classified as cavitons and disappear classified as SHFAs. The remaining 38 include cavitons that momentarily turn into SHFAs and ultimately back into cavitons (15), SHFAs that turn into cavitons (5), and SHFAs that turn into cavitons and ultimately back into SHFAs (18). For the study of the caviton-to-SHFA evolution, the first of the above-mentioned sets is chosen. Some of the structures in this set change their classification between a caviton and an SHFA multiple times (43 in total). For them, the final change of classification into an SHFA is considered to be the point when the caviton evolves into an SHFA. Comparing the amount of cavitons evolving into SHFAs to the number of "naturally" forming SHFAs (274), it is seen that slightly more SHFAs evolve from cavitons than form on their own.

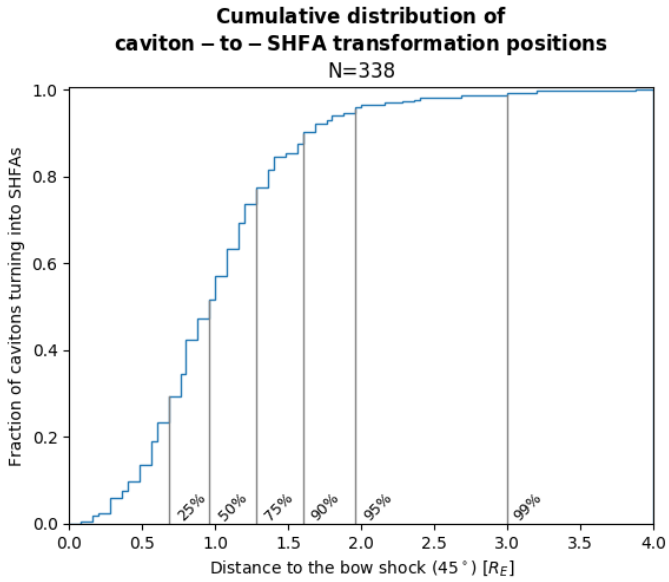

Figure 3.16: A cumulative histogram of caviton-to-SHFA transformation positions. The percentages show the fraction of all transformation taking place within that region.

Figure 3.16 shows a cumulative histogram of caviton-to-SHFA transformation positions as a function of the distance to the bow shock along the IMF, in a similar format as the histograms in Figures 3.1-3.3 shown in Section 3.2. The percentages shown in the histogram correspond to the fraction of transforming cavitons that turn into SHFAs within that distance from the bow shock. For example, within 1 R_E from the shock, 169 (50%) cavitons of the 338 transforming ones turn into SHFAs.

The shape of the distribution is very similar to the distribution of SHFA formation positions shown in Figure 3.3. The 90% marks in both distributions are roughly at the same distance ($\sim$1.6 R_E), within which 304 cavitons turn into SHFAs and 246 SHFAs form on their own. The 99% mark in the transformation distribution is located at 3.0 R_E, while it is located at $\sim$2.5 R_E in the formation distribution. Thus, SHFAs may evolve from cavitons slightly further out than where they form on their own.

Figure 3.17 depicts the transformation positions as similar heatmaps as the formation heatmaps in Figure 3.4 in Section 3.2. Comparing Figure 3.17 to the

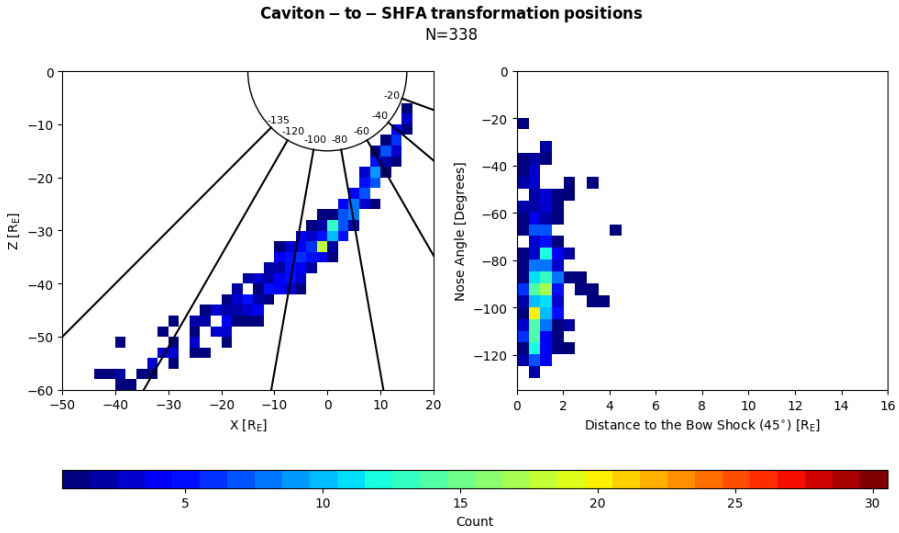

Figure 3.17: Heatmaps of caviton-to-SHFA transformation positions. Left panel: The transformation rate in Cartesian space in GSE-coordinates. Right panel: The transformation rate in the distance to the bow shock vs. nose angle coordinate system. The left panel contains an overlay showing the nose angle for easier comparison.

heatmaps of forming cavitons and SHFAs presented in Figure 3.4 shows that the transformation rate peaks at $\sim -90°$, where caviton formation is high, near, but not exactly matching the formation peak of SHFAs at $\sim -80°$. At nose angles larger than $\sim -100°$, significantly more SHFAs evolve from cavitons than form on their own. Close to the bow shock nose, at nose angles smaller than $-60°$, SHFA formation and caviton-to-SHFA evolution take place in roughly equal amounts.

4. Discussion

The tracking of cavitons and SHFAs performed in this work demonstrates that both of these structure types are commonly observed in the foreshock, with 29-72 unique structures being found at any given timestep of the tracking interval. Overall, cavitons appear to be more common than SHFAs. Roughly one-third of all cavitons evolved into SHFAs and a comparable amount of SHFAs formed on their own. Of the 1445 tracked structures, 50.5% were cavitons that did not evolve into SHFAs, 23.5% were purely SHFAs and the rest (26%) changed their classification between a caviton and an SHFA. The majority of them were cavitons that evolved into SHFAs (23.4% of all structures).

Cavitons form in a larger region than SHFAs and are more numerous of the two types. The extent of the caviton formation region appears to grow with increasing distance from the bow shock nose, but it is cut off by the simulation box boundary in this work. Because of this, the full extent of the caviton region cannot be verified.

99% of all structures formed within 10 R_E from the bow shock when the distance is measured along the field lines of the IMF (45° earthward, northward of the ecliptic). In this region, cavitons were found to form at all distances except within 0.3 R_E. SHFAs were mostly restricted to within 2.5 R_E from the shock. Within this distance, 99% of SHFA formation and ∼96% of caviton-to-SHFA evolution took place. However, cavitons also form abundantly in this "SHFA region", as 432 cavitons formed there compared to 272 naturally forming SHFAs. 210 of these

cavitons turned into SHFAs.

The results of this work can be compared to existing spacecraft observations. A statistical study of cavitons, SHFAs and other foreshock transient phenomena was conducted using observations from the Cluster spacecraft by Kajdič et al. (2017) [17]. The observational study included 92 cavitons, observed between 2001 and 2006, and 19 SHFAs, observed between 2003 and 2011. The caviton dataset was reused from an earlier statistical study involving only cavitons by Kajdič et al. (2013) [16]. The caviton criteria for the density and the magnetic field depressions in these studies are the same as in this work (number density and magnetic field magnitude less than 80% of their ambient values). In addition to these criteria, cavitons which had a different temperature than their surroundings, or had flow deflections inside them were not included in the dataset. The SHFAs included in the statistics were chosen based on visual inspection.

In the observational study of Kajdič et al. (2017), cavitons' and SHFAs' distances to the bow shock were calculated along the IMF direction, as was done in this work. The distances were obtained using a hyperboloid-shaped bow shock model, scaled with the solar wind dynamic pressure obtained from solar wind parameters near the times of each transient observation. All cavitons were observed within 9 R_E from the bow shock, and all SHFAs were observed within 6 R_E from the bow shock. The frequencies of the observations increase towards the bow shock, but the number of cavitons drops at <1 R_E. These observations indicate a similar caviton/SHFA region as found in this work, but the SHFA region resolved from the Cluster data is twice as large. However, the observational study spans a large time period and includes observations for different solar wind conditions which is not done in this work. Presumably the size of the SHFA region changes with the solar wind conditions and the conditions in the foreshock. A matter to consider when using the distance measurement along the IMF direction is that the measured distance to the

bow shock is affected by the orientation of the IMF. Due to the geometry of the bow shock, different distance ranges may be obtained for different IMF orientations.

The most distinct features of cavitons and SHFAs, the simultaneous depressions of particle number density and magnetic field magnitude, were evaluated in this work by looking at the minima of these parameters over each structure's lifetime. The correlation between the minima of the density and the magnetic field was calculated by taking the overall density minimum for each structure and plotting the structures' magnetic field minimum from the same timestep against it. The depressions appear well correlated inside cavitons (correlation coefficient $C = 0.793$) and show some correlation inside SHFAs, but with significantly more spread ($C = 0.575$). The observational studies by Kajdič et al. (2013, 2017) also found a good correlation between the depressions inside cavitons, with a correlation coefficient of 0.85. Similar to this work, the correlation was found to be worse inside SHFAs, with a correlation coefficient of 0.30. However, the SHFA statistics only include 19 observations.

The simultaneous depressions of the total proton number density and the magnetic field magnitude appear equally deep inside cavitons in this work. By comparing the "pure" sets containing the cavitons that did not evolve into SHFAs and the SHFAs that did not evolve from cavitons, it was seen that SHFAs tend to have larger depressions in the density and the magnetic field. For cavitons, the largest deviation from the solar wind proton number density is 26.8% on average, and the largest deviation from the solar wind magnetic field magnitude is 26.5% on average. For SHFAs, the corresponding values are 33.6% and 36.6%. Overall, the most depleted structures on average were the ones that evolved from cavitons into SHFAs (38.4%, 39.9%). The large depressions inside these structures could occur as already depleted, well-developed cavitons approach the bow shock, turn into SHFAs and experience further depletion of density and magnetic field magnitude in their interiors.

It should however be noted that compared to results from observational studies, the depressions of density and magnetic field found here appear shallow. In Kajdič et al. (2017), cavitons were reported to have average density and magnetic field depressions of 50%, around which values are evenly distributed within 20%-80%. The distributions for both cavitons and SHFAs presented by Kajdič et al. (2017) appear different to the ones in this work. Here the depressions of total proton number density and the magnetic field magnitude were found to rarely exceed 50%, especially in the case of cavitons. As for the shallow structures, which were found abundantly in this work, it must be noted that such, small cavitons or SHFAs might not even be resolvable from spacecraft data, since the structures are surrounded by ULF waves. Then again, the threshold used in this work for density and magnetic field depressions is compared to the ambient solar wind and not the vicinity of the structures. The conditions in the foreshock differ from the constant, upstream solar wind values, and the depressions may appear shallow because of this.

Inside SHFAs, the slightly larger deviation of the magnetic field magnitude compared to the proton number density and the weaker correlation between these parameters can be explained by the high concentrations of suprathermal protons. This was seen by excluding the suprathermal population's contribution to the correlation between density and magnetic field. The correlation coefficient for cavitons was virtually unaffected ($C = 0.79$), whereas for SHFAs the coefficient climbed to 0.695. The average depression inside SHFAs is very high, 90%. The distribution for SHFAs is heavily peaked at these very large depressions.

For a structure to qualify as an SHFA in this work, a requirement of β>10 in at least 60% of a structure's cells was set. This criterion appears to be suitable, based on the evaluation of suprathermal density, temperature and bulk flow speed distributions of cavitons and SHFAs. Two distinct populations, corresponding to cavitons and SHFAs, are clearly visible in the suprathermal density and temperature distri-

butions. Cavitons appear strongly peaked around low suprathermal densities, low temperatures and near-solar wind bulk flow speeds. The SHFA distributions display a larger spread, but have distinctive higher suprathermal density, temperature and lower bulk flow speeds. Most notably a clear switch from cavitons to SHFAs occurs in the maximum temperature, at ∼7 MK.

In the case of bulk flow speeds, the maximum slowdown of solar wind bulk flow speed (750 km/s) inside pure cavitons shows an average value of 5.7% and inside pure SHFAs an average value of 20.0%. With all structures included, the average value is 12.2%. The minimum bulk flow speed distribution of SHFAs shows that slowdowns of ∼40% (down to 450 km/s) are not uncommon. The largest slowdown was ∼66%, although values above 45% were rare. The deviation from the solar wind value commonly exceeds 20% inside SHFAs, but rarely inside cavitons.

The bulk flow speeds of SHFAs were also evaluated by Kajdič et al. (2017). This was not done for cavitons, as it was required for them to have no reduction in bulk flow speed. SHFAs exhibited an average slowdown of 60% from the solar wind flow speed, with a mostly uniform distribution from 30% to 100%. Similar to the depressions of density and magnetic field, the deviations of bulk flow inside SHFAs appear stronger in spacecraft data than in this computational work.

As was noted in the previous chapter, the apparent reduction in bulk flow speed is explained as an effect of two counterstreaming populations, which are the solar wind core and the reflected suprathermal ions. The simultaneous reduction of the core density and increase of the suprathermal ion density results in an apparent slowdown of the bulk flow speed, since the speed is calculated as the weighted average of velocity over the entire velocity space with the ion number densities as the weights (Parks et al., 2017) [34]. This interpretation is supported by the strong correlation between bulk flow speed minima and suprathermal number density maxima ($C = -0.81$), which shows that the bulk flow speed decreases with the increasing

suprathermal number density.

Cavitons appear to be larger in size than SHFAs in this work. For pure cavitons, the average maximum area was 0.114 R_E^2 and the median maximum area was 0.062 R_E^2. The average and median values for pure SHFAs were 0.076 R_E^2 and 0.040 R_E^2. The largest structures were those which changed their categorization between a caviton and an SHFA. For them the average maximum area was 0.269 R_E^2 and the median maximum area 0.171 R_E^2. The small sizes of SHFAs are most likely due to their proximity to the bow shock, which restricts them from growing before they arrive to the shock edge.

In Kajdič et al. (2013), spatial extents of cavitons observed by Cluster were calculated by multiplying the durations of the cavitons in spacecraft data with the solar wind speed. There the extents of the cavitons were found to range between 1-13 R_E with average and median values of 4.6 R_E and 4.1 R_E. The most common extents were between 3-5 R_E, including 61% of cavitons. As cavitons are found to move slightly slower than the solar wind, this method is not entirely accurate and overestimates the structure sizes, but will serve as a rough estimate. Nonetheless, the observed extents appear notably larger than the extents implied by the areas found in this work. By approximating the structures in this work to be square-shaped, the side length calculated from the average maximum area (0.1445 R_E^2 for all structures) is 0.38 R_E. In Kajdič et al. (2017), the durations of SHFAs in spacecraft data were found to be similar to the durations of cavitons.

One source contributing to the difference in the extents is that Kajdič et al. (2013) have included the rims of enhanced density/magnetic field surrounding the cavitons to the caviton duration, which is not done here. In the study by Blanco-Cano et al. (2018) [4], which used the same Vlasiator run as this work, it was noted that these rims are not as prominent in Vlasiator as in spacecraft observations. This was believed to be an effect of the simulation's spatial resolution, which can

limit the steepening of ULF waves (Pfau-Kempf et al., 2018) [40]. This could also limit the growth of cavitons and SHFAs. Furthermore, like with the shallow density and magnetic field depressions, short duration structures surrounded by ULF fluctuations might also be difficult to recognize from spacecraft data.

The properties of cavitons and SHFAs appear to vary with their position in the foreshock. The most significant variation was as a function of distance to the bow shock, which showed that there are deeper density and magnetic field depressions, higher temperatures, slower bulk flow speeds and larger structures with the decreasing distance to the bow shock. The suprathermal density appears to rise only very close to the bow shock. Larger depressions near the bow shock have been previously observed in numerical studies by Blanco-Cano et al. (2009, 2011) [6][5] and the results obtained in this thesis support this picture.

The variation of the properties is much less significant as a function of the nose angle. For cavitons, the structure sizes showed a slight dependence on the nose angle, since the largest cavitons were found where the formation region extends furthest away from the bow shock. Some trends were seen for SHFAs, such as higher temperatures and slightly slower bulk flow speeds near the bow shock nose, and larger magnetic field depressions far from the bow shock nose. It was also seen in Section 3.2 that the SHFA formation rate drops with increasing nose angle. Although cavitons form abundantly at large nose angles, only a small fraction of them appear to transform into SHFAs.

The variation of SHFAs' properties with the nose angle shows good agreement with the results obtained by Omidi et al. (2014a) [30], who studied the parametric dependencies of SHFAs with a global hybrid simulation as a function of Alfvén Mach number, IMF cone angle and latitude from the Sun-Earth line. They found a clear latitude dependence for temperature, bulk flow speed reduction and SHFA occurrence. Like in this work, temperatures were higher, bulk flow speeds lower

and SHFAs were observed more abundantly at low latitudes than high latitudes. Omidi et al. (2014a) also found out that these trends became more pronounced with increasing Alfvén Mach number.

For the propagation speed of cavitons and SHFAs, a clear value was obtained in this work. Both cavitons and SHFAs were found to propagate at an earthward speed of ∼606 km/s. In the solar wind rest frame, the speed is ∼144 km/s towards the Sun. This value compares well to spacecraft observations. Kajdič et al. (2011) [18] calculated the propagation speeds in the solar wind rest frame for two cavitons observed by Cluster, and obtained values of 188 km/s and 120 km/s in the sunward direction. The solar wind flow speeds measured during the cavitons observed by Kajdič et al. (2011) were however smaller than in the simulation run used in this work, 377 km/s and 518 km/s along the Sun-Earth line. Here a value was also obtained for the speed out of ecliptic, which is ∼-110 km/s southward, calculated using all structures. The southward propagation speed appears to be slightly larger for SHFAs than cavitons (101 km/s with "pure" cavitons only, 156 km/s with "pure" SHFAs only).

The solar wind magnetosonic speed in the studied simulation run is ∼134 km/s (M_{ms}=5.6), which suggests that the overall propagation speed of cavitons and SHFAs in the solar wind rest frame ($|v| \simeq$ 181 km/s) is supermagnetosonic. To investigate the origin of cavitons' and SHFAs' sunward and southward propagation, the $\mathbf{E} \times \mathbf{B}$-drift velocity caused by the solar wind convection electric field was calculated for v_{sw}=(-750,0,0) km/s and B=($\frac{5}{\sqrt{2}}$,0,$-\frac{5}{\sqrt{2}}$) nT. The resulting drift velocity is $\mathbf{v_{E\times B}}$ = (-375,0,-375) km/s, corresponding to a total speed $|\mathbf{v_{E\times B}}|$ = 530.33 km/s directed towards Earth and south of the ecliptic at a 45° angle. In both the x- and the z-direction, the drift speed is significantly higher than the propagation speed calculated for the structures. Furthermore, the x-directional drift velocity is directed towards Earth, disagreeing with the sunward propagation in the solar wind

rest frame. Since the above values are calculated for the ambient solar wind, they do not fully account for the conditions in the foreshock where the flow is perturbed by backstreaming ions. Especially for the magnetosonic speed, a more detailed analysis using averaged values from the foreshock would be more suitable.

5. Summary and conclusions

In this thesis, two foreshock transient types, cavitons and spontaneous hot flow anomalies (SHFAs) were studied statistically using the global magnetospheric simulation Vlasiator. Simulations are well suited for such statistical studies, as they provide a global picture, a feat that cannot be accomplished with spacecraft observations, which are limited to point observations. Statistical studies conducted with simulations have the benefit of being able to produce large statistics. In spacecraft observations, gathering statistics takes years, and the solar wind conditions vary vastly in the sample. In simulations, the parameters of the solar wind and the IMF can be controlled, which grants a clean statistical sample and makes the results straightforward to analyze.

To fully utilize the advantages provided by Vlasiator, individual transients were tracked in this work. For this purpose, a tracking algorithm was developed. Tracking transients in the simulation allowed obtaining a large set of statistics about details that are difficult to observe with spacecraft, such as transient formation, evolution and propagation. In this work, cavitons and SHFAs were tracked in a single Vlasiator simulation run for a total duration of 537.5 s, producing a sample of 1445 transients. The following conclusions can be made based on this study:

1. The transients studied in the simulation run fit well the description of cavitons and SHFAs established in the existing literature. Cavitons have equally large, well correlated depressions in the plasma density and the magnetic field

magnitude. In addition to these properties, SHFAs exhibit significant heating and bulk flow deflection inside them. These properties are well correlated with the amount of suprathermal ions, which is low inside cavitons but can reach high values inside SHFAs.

2. On average, SHFAs have larger density and magnetic field depressions inside them than cavitons. The average deviations from the solar wind values are 26.8% and 26.5% inside cavitons and 33.6% and 36.6% inside SHFAs. The depressions are shallow compared to earlier studies where deviations larger than 50% from the solar wind values are common.

3. Caviton formation in the foreshock is uniform and abundant within $\sim$6 R_E from the bow shock. The extent of the caviton formation region increases when moving further away from the shock nose. Beyond 10 R_E caviton formation is scarce. SHFAs are found at distances closer than $\sim$ 3.5 R_E from the bow shock. The results are comparable with spacecraft statistics, in which cavitons have been observed within 9 R_E and SHFAs within 6 R_E from the shock.

4. SHFAs can either form on their own or evolve from cavitons. Roughly a third of all tracked cavitons turn into SHFAs. SHFA formation decreases with the increasing latitude from the bow shock nose, agreeing with earlier numerical studies.

5. Approaching the bow shock, the density and magnetic field depressions inside transients deepen. At the same time, the temperatures increase and the bulk flow speeds slow down. Caviton properties do not show significant variation with the nose angle/latitude. SHFAs have higher temperatures and slower bulk flow speeds close to the bow shock nose and their magnetic field depressions deepen far away from the nose.

6. Cavitons and SHFAs propagate sunwards in the solar wind rest frame with an uniform speed of $\sim$ 144 km/s, which is validated by the excellent correlation between transient lifetime and propagation distance. The propagation velocity also has a southward component, with a speed of $\sim$ 110 km/s. The southward speed is somewhat larger for SHFAs compared to cavitons. The sunward propagation speed agrees well with the spacecraft observations, where speeds of 188 km/s and 120 km/s have been measured.

A difference between the results of this study and spacecraft observations is the size of transients. The transients studied in this work are significantly smaller than those observed by spacecraft. The smaller sizes of the transients alongside with the shallower density and magnetic field depressions are most likely due to the limited spatial resolution and the field solver of the simulation, which both tend to reduce the steepening of waves and structures in the simulation. However, for other transient properties, and particularly for the transient propagation speed, good agreement is found between this numerical study and past observational and numerical studies.

The results of this study have demonstrated that global hybrid-Vlasov simulations of Earth's magnetosphere can be used to supplement spacecraft observations of foreshock transients. The next step would be to gather statistics from simulation runs with different conditions. Such study would help to establish how cavitons' and SHFAs' properties depend on the solar wind and the IMF. It would also allow for a more detailed comparison with spacecraft statistics, which consist of observations with vastly varying solar wind conditions. As for numerical studies, the caviton and SHFA criteria used in this work appear to reproduce the properties of the transients accurately. In future studies, additional work could be done to improve the criteria, so that they would better suit the varying conditions in the foreshock.

The methodology developed in this work has been shown to be practical for

studying foreshock transients in large quantities. Tracking cavitons and SHFAs has allowed conducting study of their evolution, which is largely impractical in obervational studies. The tracking scheme of this work can be very easily be adapted for tracking and conducting statistics of different types of foreshock transients as well, and it could also find use in other types of numerical studies.

Acknowledgements

For making this work possible, the author of this thesis acknowledges the European Research Council for Starting grant 200141-QuESpace, with which Vlasiator was developed, and Consolidator grant 682068-PRESTISSIMO awarded to further develop Vlasiator and use it for scientific investigations. The Finnish Centre of Excellence in Research of Sustainable Space, funded through the Academy of Finland grant number 312351, supports Vlasiator development and science as well. Also acknowledged are the grant numbers 309937 and 322544 of the Academy of Finland. The CSC-IT Center for Science in Finland is acknowledged for the Sisu supercomputer pilot usage and Grand Challenge award leading to the results presented here.

The author also thanks the supervisors and censors of this thesis, Dr. Lucile Turc, Dr. Markus Battarbee and prof. Minna Palmroth for their support and helpful comments during the preparation of this thesis, and the author's parents, Ilkka and Pia Tarvus, for reminding to go outdoors once in a while.

A. Algorithm for tracking transient structures

In this Appendix, an outline is presented for the completed transient tracking algorithm, that can be used to track moving structures such as cavitons and SHFAs, utilizing the techniques presented in Chapter 2.

The result of the tracking is controlled by three parameters. They are the percentage of overlap between related structures, the minimum cell count of structures and the time limit for tracking disappeared structures.

The output consists of three files per tracked structure. The first contains the timesteps during which the structure was tracked, the second the cells of the structure at the respective times, and the third the parent of the structure at the respective times. Each tracked structure is identified with a unique ID number, which is used also for the identification of parents.

In the algorithm, the tracked structures are implemented as a custom class. Their attributes include ID, the cells at each timestep, the parent ID at each timestep, the corresponding timesteps, and two separate stacks for children (upstream and downstream). The class contains three class methods, which are shown below.

- **Update(cells, timestep, parent ID)**: Update a structure and all its children with given **cells**, **timestep** and **parent ID**.
- **Merge(structure, cells)**: Put the given **structure** to either list of children. The relevant list is chosen by comparing **structures** latest cells' mean x-coordinate to mean x-coordinate of **cells**.
- **Split(cells)**: Pop and return a structure from either list of children. The relevant list is chosen by comparing **structures** latest cells' mean x-coordinate to mean x-coordinate of **cells**. If list is empty, return a copy of parent without children, with a new ID.

Below is the pseudocode outline for the algorithm. Its operation is primarily based on utilization of five different arrays. **tracked_list** contains all currently tracked structures. **old_events** contains the cells of each static structure found at timestep N, and **new_events** the cells of each static structure at timestep N+1. **old_pointers** and **new_pointers** have the same size and indexing as the corresponding **events**-array. Each value of **pointers**-array is either NULL or "points" to an index of **tracked_list**. The purpose of the pointers is to tell which static structure belongs to which tracked structure, as the relations are being resolved. After all relations have been resolved, the remaining NULL values indicate static structures that did not become a part of any tracked structure. Here, the indexing of arrays is assumed to start from zero.

1. Initialize arrays **tracked_list** and **disappeared_list** for tracked and disappeared structures
2. Read the cells of separate structures at the first timestep to array **old_events**, exclude all structures under minimum size

3. Repeat between all timesteps N and N+1 of the tracking interval:

    3.1. Read the size of **tracked_structures** into variable **n_tracked**

    3.2. Append the latest cells from all structures in **tracked_list** to the front of **old_events**

    3.3. Read the cells of separate structures at timestep N+1 to array **new_events**, exclude all structures under minimum size

    3.4. Initialize **old_pointers**, an array of NULLs with the size of **old_events**

    3.5. Initialize **new_pointers**, an array of NULLs with the size of **new_events**

    3.6. Iterate through **old_events** in order of decreasing structure size, denote the index with **i**

        3.6.1. Iterate through **new_events** in order of decreasing structure size, denote the index with **j**

            3.6.1.1. Count the number of intersecting cells between **old_events[i]** and **new_events[j]**

            3.6.1.2. If the overlap is smaller than a fixed percentage of smaller structure's cell count, skip to the next iteration

            3.6.1.3. Check values of **old_pointers[i]** and **new_pointers[j]**, perform an operation based on the truth table in Table A.1

                - TRANSLATE:
                    - If **i<n_tracked**, set **old_pointers[i]** and **new_pointers[j]** to value **i**
                    - Else, set **old_pointers[i]** and **new_pointers[j]** to the size of **tracked_list**,

                      create a new structure with **old_events[i]** and timestep N, append to **tracked_list**

- MERGE:
  - If **i<n_tracked**, set **old_pointers[i]** to value **i**
  - Else, set **old_pointers[i]** to the size of **tracked_list**, create a new structure with **old_events[i]** and timestep N, append to **tracked_list**
  - Merge **tracked_list[old_pointers[i]]** to **tracked_list[new_pointers[j]]**
- SPLIT:
  - Set **new_pointers[j]** to the size of **tracked_list**
  - Split a structure from **tracked_list[old_pointers[i]]** with cells of **new_events[j]**
  - Append the split structure to **tracked_list**
- PARTIAL SPLIT:
  - Do nothing

3.7. Empty **old_events**

3.8. Iterate through **new_pointers** with index **i**

- If **new_pointers[i]** is NULL, append **new_events[i]** to **old_events**
- Else, update **tracked_list[new_events[i]]** with cells of **new_events[i]**, timestep N+1 and its own ID as the parent

3.9. Iterate through **tracked_list** in reverse order with index **i**

- If **i** is not in **new_pointers**, but is in **old_pointers**, delete **tracked_list[i]**
- If **i** is not in **new_pointers** and not in **old_pointers**, check if **tracked_list[i]** is older than set time limit
  - If it is, append to **disappeared_list** and delete **tracked_list[i]**

4. Create outputs for all structures in **tracked_list** and **disappeared_list**

Old pointer = NULL	New pointer = NULL	Operation
T	T	TRANSLATE
T	F	MERGE
F	T	SPLIT
F	F	PARTIAL SPLIT

Table A.1: Truth table of possible operations for above algorithm.

During an iteration, a NULL value in Table A.1 means that the old/new static structure hasn't been visited yet. When the old and new structures are compared in descending order of size as in step 3.6, Table A.1 is actually a compact representation of rules defined in section 2.3.1.

The key is to note that whenever the first relation of a structure is found, it is automatically the one with the largest of the structures it is related to. This guarantees that when both related structures are visited for the first time, they are the largest structures related to each other and fulfill rule 2a). If a structure at timestep N (denoted A) is visited for the first time, but the structure at timestep N+1 (denoted B) is not, it must be so that A is not the largest structure related to B and rule 2b) is fulfilled. In the opposite case, where structure B is visited for the first time, it can't be the largest structure related to A and rule 3a) is fulfilled. Finally, if both structures have already been visited before, they fulfill rule 3b). Hence, iterating over the structures by size in descending order gives the correct type of relation in all situations.

Another matter that is not immediately evident from the algorithm is how the splitting and merging structures are split/merged from/into correct structures, simultaneously avoiding NULL pointers. A merging structure is merged into structure at index **new_pointers[j]** of **tracked_list**, under step 3.6.1.3. But, as can be deduced from table A.1, the structure at index **j** of **new_events** must have

been already visited. This implies that the structure exists in the **tracked_list**, so the merging is carried out validly. The same applies for splitting events. There, it is guaranteed that structure at index **old_pointers[i]** exists in **tracked_list**, as index **i** of **old_events** has been visited earlier.

The actual updating of all tracked structures is carried out at the end of each timestep since then all structures have merged/split correctly. This is done in step 3.8, in which also all non-matched static structures from **new_events** are transferred to **old_events** for the next timestep. The purpose of the first if-clause in step 3.9 is to remove all old merged structures from tracking. They can be easily identified because they only have the old pointer set.

References

1 M. O. Archer, D. L. Turner, J. P. Eastwood, S. J. Schwartz, and T. S. Horbury. Global impacts of a Foreshock Bubble: Magnetosheath, magnetopause and ground-based observations. *Planetary and Space Science*, 106:56–66, Feb 2015.

2 M. Battarbee, U. Ganse, Y. Pfau-Kempf, L. Turc, T. Brito, M. Grandin, T. Koskela, and M. Palmroth. Non-locality of the earth's quasi-parallel bow shock: injection of thermal protons in a hybrid-vlasov simulation. *Annales Geophysicae Discussions*, 2019:1–26, 2019.

3 Wolfgang Baumjohann and Rudolf A. Treumann. *Basic space plasma physics*. 1996.

4 X. Blanco-Cano, M. Battarbee, L. Turc, A. P. Dimmock, E. K. J. Kilpua, S. Hoilijoki, U. Ganse, D. G. Sibeck, P. A. Cassak, R. C. Fear, R. Jarvinen, L. Juusola, Y. Pfau-Kempf, R. Vainio, and M. Palmroth. Cavitons and spontaneous hot flow anomalies in a hybrid-vlasov global magnetospheric simulation. *Annales Geophysicae*, 36(4):1081–1097, 2018.

5 X. Blanco-Cano, P. Kajdič, N. Omidi, and C. T. Russell. Foreshock cavitons for different interplanetary magnetic field geometries: Simulations and observations. *Journal of Geophysical Research (Space Physics)*, 116(A9):A09101, Sep 2011.

6 X. Blanco-Cano, N. Omidi, and C. T. Russell. Global hybrid simulations: Foreshock waves and cavitons under radial interplanetary magnetic field geometry. *Journal of Geophysical Research (Space Physics)*, 114(A1):A01216, Jan 2009.

7 David Burgess and Manfred Scholer. *Collisionless Shocks in Space Plasmas*. 2015.

8 Steven R. Cranmer, Sarah E. Gibson, and Pete Riley. Origins of the Ambient Solar Wind: Implications for Space Weather. *Space Science Reviews*, 212(3-4):1345–1384, Nov 2017.

9 J. P. Eastwood, E. A. Lucek, C. Mazelle, K. Meziane, Y. Narita, J. Pickett, and R. A. Treumann. The Foreshock. *Space Science Reviews*, 118(1-4):41–94, Jun 2005.

10 J. P. Edmiston and C. F. Kennel. A parametric survey of the first critical Mach number for a fast MHD shock. *Journal of Plasma Physics*, 32(3):429–441, December 1984.

11 G. Facskó, Z. Németh, G. Erdos, A. Kis, and I. Dandouras. A global study of hot flow anomalies using Cluster multi-spacecraft measurements. *Annales Geophysicae*, 27(5):2057–2076, May 2009.

12 S. A. Fuselier. Ion distributions in the Earth's foreshock upstream from the bow shock. *Advances in Space Research*, 15(8-9):43–52, Jan 1995.

13 S. A. Fuselier, M. F. Thomsen, J. T. Gosling, S. J. Bame, and C. T. Russell. Gyrating and intermediate ion distributions upstream from the earth's bow shock. *Journal of Geophysical Research*, 91(A1):91–100, Jan 1986.

14 E. W. Greenstadt, G. Le, and R. J. Strangeway. ULF waves in the foreshock. *Advances in Space Research*, 15(8-9):71–84, Jan 1995.

15 H. Hietala, T. V. Laitinen, K. Andréeová, R. Vainio, A. Vaivads, M. Palmroth, T. I. Pulkkinen, H. E. J. Koskinen, E. A. Lucek, and

H. Rème. Supermagnetosonic Jets behind a Collisionless Quasiparallel Shock. *Physical Review Letters*, 103(24):245001, Dec 2009.

16 P. Kajdič, X. Blanco-Cano, N. Omidi, K. Meziane, C. T. Russell, J.-A. Sauvaud, I. Dandouras, and B. Lavraud. Statistical study of foreshock cavitons. *Annales Geophysicae*, 31(12):2163–2178, 2013.

17 P. Kajdič, X. Blanco-Cano, N. Omidi, D. Rojas-Castillo, D. G. Sibeck, and L. Billingham. Traveling Foreshocks and Transient Foreshock Phenomena. *Journal of Geophysical Research (Space Physics)*, 122(9):9148–9168, Sep 2017.

18 Primož Kajdič, Xochitl Blanco-Cano, Nojan Omidi, and Christopher T. Russell. Multi-spacecraft study of foreshock cavitons upstream of the quasi-parallel bow shock. *Planetary and Space Science*, 59(8):705–714, Jun 2011.

19 F. T. Katırcıoğlu, Z. Kaymaz, D. G. Sibeck, and I. Dandouras. Magnetosheath cavities: case studies using Cluster observations. *Annales Geophysicae*, 27(10):3765–3780, Oct 2009.

20 Yann Kempf, Dimitry Pokhotelov, Olga Gutynska, III Wilson, Lynn B., Brian M. Walsh, Sebastian von Alfthan, Otto Hannuksela, David G. Sibeck, and Minna Palmroth. Ion distributions in the Earth's foreshock: Hybrid-Vlasov simulation and THEMIS observations. *Journal of Geophysical Research (Space Physics)*, 120(5):3684–3701, May 2015.

21 Kenneth R. Lang. *Essential Astrophysics*. 2013.

22 Y. Lin. Global-scale simulation of foreshock structures at the quasi-parallel bow shock. *Journal of Geophysical Research (Space Physics)*, 108(A11):1390, Nov 2003.

23 Y. Lin and X. Y. Wang. Three-dimensional global hybrid simulation of dayside dynamics associated with the quasi-parallel bow shock. *Journal of Geophysical Research (Space Physics)*, 110(A12):A12216, Dec 2005.

24 K. Meziane and C. D'Uston. A statistical study of the upstream intermediate ion boundary in the Earth's foreshock. *Annales Geophysicae*, 16(2):125–133, Feb 1998.

25 N. Omidi. Formation of cavities in the foreshock. In Dastgeer Shaikh and Gary P. Zank, editors, *Turbulence and Nonlinear Processes in Astrophysical Plasmas*, volume 932 of *American Institute of Physics Conference Series*, pages 181–190, Aug 2007.

26 N. Omidi, J. Berchem, D. Sibeck, and H. Zhang. Impacts of spontaneous hot flow anomalies on the magnetosheath and magnetopause. *Journal of Geophysical Research (Space Physics)*, 121(4):3155–3169, Apr 2016.

27 N. Omidi, J. P. Eastwood, and D. G. Sibeck. Foreshock bubbles and their global magnetospheric impacts. *Journal of Geophysical Research (Space Physics)*, 115(A6):A06204, Jun 2010.

28 N. Omidi, D. Sibeck, O. Gutynska, and K. J. Trattner. Magnetosheath filamentary structures formed by ion acceleration at the quasi-parallel bow shock. *Journal of Geophysical Research (Space Physics)*, 119(4):2593–2604, Apr 2014.

29 N. Omidi, D. G. Sibeck, and X. Blanco-Cano. Foreshock compressional boundary. *Journal of Geophysical Research (Space Physics)*, 114(A8):A08205, Aug 2009.

30 N. Omidi, H. Zhang, C. Chu, D. Sibeck, and D. Turner. Parametric dependencies of spontaneous hot flow anomalies. *Journal of Geophysical Research (Space Physics)*, 119(12):9823–9833, Dec 2014.

31 N. Omidi, H. Zhang, D. Sibeck, and D. Turner. Spontaneous hot flow anomalies at quasi-parallel shocks: 2. Hybrid simulations. *Journal of Geophysical Research (Space Physics)*, 118(1):173–180, Jan 2013.

32 Minna Palmroth, Urs Ganse, Yann Pfau-Kempf, Markus Battarbee, Lucile Turc, Thiago Brito, Maxime Grandin, Sanni Hoilijoki, Arto Sandroos, and Sebastian von Alfthan. Vlasov methods in space physics and astrophysics. *Living Reviews in Computational Astrophysics*, 4(1):1, Aug 2018.

33 E. N. Parker. Dynamics of the Interplanetary Gas and Magnetic Fields. *The Astrophysical Journal*, 128:664, Nov 1958.

34 G. K. Parks, E. Lee, S. Y. Fu, N. Lin, Y. Liu, and Z. W. Yang. Shocks in collisionless plasmas. *Reviews of Modern Plasma Physics*, 1(1):1, Dec 2017.

35 G. K. Parks, E. Lee, N. Lin, F. Mozer, M. Wilber, E. Lucek, I. Dandouras, H. Rème, J. B. Cao, P. Canu, N. Cornilleau-Wehrlin, P. Décréau, M. L. Goldstein, and Philippe Escoubet. Density holes in the upstream solar wind. In Dastgeer Shaikh and Gary P. Zank, editors, *Turbulence and Nonlinear Processes in Astrophysical Plasmas*, volume 932 of *American Institute of Physics Conference Series*, pages 9–15, Aug 2007.

36 G. K. Parks, E. Lee, F. Mozer, M. Wilber, E. Lucek, I. Dandouras, H. Rème, C. Mazelle, J. B. Cao, K. Meziane, M. L. Goldstein, and

P. Escoubet. Larmor radius size density holes discovered in the solar wind upstream of Earth's bow shock. *Physics of Plasmas*, 13(5):050701, May 2006.

37 G. Paschmann, N. Sckopke, S. J. Bame, J. R. Asbridge, J. T. Gosling, C. T. Russell, and E. W. Greenstadt. Association of low-frequency waves with suprathermal ions in the upstream solar wind. *Geophysical Research Letters*, 6(3):209–212, Mar 1979.

38 G. Paschmann, N. Sckopke, I. Papamastorakis, J. R. Asbridge, S. J. Bame, and J. T. Gosling. Characteristics of reflected and diffuse ions upstream from the earth's bow shock. *Journal of Geophysical Research*, 86(A6):4355–4364, Jun 1981.

39 Götz Paschmann and Patrick W. Daly. Analysis Methods for Multi-Spacecraft Data. ISSI Scientific Reports Series SR-001, ESA/ISSI, Vol. 1. ISBN 1608-280X, 1998. *ISSI Scientific Reports Series*, 1, January 1998.

40 Yann Pfau-Kempf, Markus Battarbee, Urs Ganse, Sanni Hoilijoki, Lucile Turc, Sebastian von Alfthan, Rami Vainio, and Minna Palmroth. On the importance of spatial and velocity resolution in the hybrid-Vlasov modeling of collisionless shocks. *Frontiers in Physics*, 6:44, May 2018.

41 C. T. Russell and M. M. Hoppe. Upstream Waves and Particles. *Space Science Reviews*, 34(2):155–172, Feb 1983.

42 Steven J. Schwartz and David Burgess. Quasi-parallel shocks: A patchwork of three-dimensional structures. *Geophysical Research Letters*, 18(3):373–376, Mar 1991.

43 Steven J. Schwartz, David Burgess, William P. Wilkinson, Ramona L. Kessel, Malcolm Dunlop, and Herman Luehr. Observations of Short Large-Amplitude Magnetic Structures at a Quasi-Parallel Shock. *Journal of Geophysical Research*, 97(A4):4209–4227, Apr 1992.

44 Steven J. Schwartz, Chris P. Chaloner, Peter J. Christiansen, Andrew J. Coates, David S. Hall, Alan D. Johnstone, M. Paul Gough, Andrew J. Norris, Richard P. Rijnbeek, David J. Southwood, and Les J. C. Woolliscroft. An active current sheet in the solar wind. *Nature*, 318(6043):269–271, Nov 1985.

45 Steven J. Schwartz, David Sibeck, Mark Wilber, Karim Meziane, and Timothy S. Horbury. Kinetic aspects of foreshock cavities. *Geophysical Research Letters*, 33(12):L12103, Jun 2006.

46 J. H. Shue, J. K. Chao, H. C. Fu, C. T. Russell, P. Song, K. K. Khurana, and H. J. Singer. A new functional form to study the solar wind control of the magnetopause size and shape. *Journal of Geophysical Research*, 102(A5):9497–9512, May 1997.

47 J. H. Shue, P. Song, C. T. Russell, J. T. Steinberg, J. K. Chao, G. Zastenker, O. L. Vaisberg, S. Kokubun, H. J. Singer, T. R. Detman, and H. Kawano. Magnetopause location under extreme solar wind conditions. *Journal of Geophysical Research*, 103(A8):17691–17700, August 1998.

48 D. G. Sibeck, N. Omidi, I. Dandouras, and E. Lucek. On the edge of the foreshock: model-data comparisons. *Annales Geophysicae*, 26(6):1539–1544, Jun 2008.

49 D. G. Sibeck, T. D. Phan, R. Lin, R. P. Lepping, and A. Szabo. Wind

observations of foreshock cavities: A case study. *Journal of Geophysical Research (Space Physics)*, 107(A10):1271, Oct 2002.

50 V. A. Thomas and Stephen H. Brecht. Evolution of diamagnetic cavities in the solar wind. *Journal of Geophysical Research*, 93(A10):11341–11353, Oct 1988.

51 M. F. Thomsen, V. A. Thomas, D. Winske, J. T. Gosling, M. H. Farris, and C. T. Russell. Observational test of hot flow anomaly formation by the interaction of a magnetic discontinuity with the bow shock. *Journal of Geophysical Research*, 98(A9):15319–15330, Sep 1993.

52 R. A. Treumann. Fundamentals of collisionless shocks for astrophysical application, 1. Non-relativistic shocks. *The Astronomy and Astrophysics Review*, 17(4):409–535, December 2009.

53 R.A. Treumann and M. Scholer. The magnetosphere as a plasma laboratory. In J.A.M. Bleeker, J. Geiss, and Huber M.C.E., editors, *Century of Space Science*. Springer,Dordrecht, 2001.

54 D. L. Turner, N. Omidi, D. G. Sibeck, and V. Angelopoulos. First observations of foreshock bubbles upstream of Earth's bow shock: Characteristics and comparisons to HFAs. *Journal of Geophysical Research (Space Physics)*, 118(4):1552–1570, Apr 2013.

55 S. von Alfthan, D. Pokhotelov, Y. Kempf, S. Hoilijoki, I. Honkonen, A. Sandroos, and M. Palmroth. Vlasiator: First global hybrid-vlasov simulations of earth's foreshock and magnetosheath. *Journal of Atmospheric and Solar-Terrestrial Physics*, 120:24 – 35, 2014.

56 L. B. Wilson. Low Frequency Waves at and Upstream of Collision-

less Shocks. *Washington DC American Geophysical Union Geophysical Monograph Series*, 216:269–291, Feb 2016.

57 L. B. Wilson, D. G. Sibeck, A. W. Breneman, O. Le Contel, C. Cully, D. L. Turner, V. Angelopoulos, and D. M. Malaspina. Quantified energy dissipation rates in the terrestrial bow shock: 1. Analysis techniques and methodology. *Journal of Geophysical Research (Space Physics)*, 119(8):6455–6474, Aug 2014.

58 Daniel Winterhalter and Margaret G. Kivelson. Observations of the Earth's bow shock under high Mach number/high plasma beta solar wind conditions. *Geophysical Research Letters*, 15(10):1161–1164, Sep 1988.

59 H. Zhang, D. G. Sibeck, Q. G. Zong, N. Omidi, D. Turner, and L. B. N. Clausen. Spontaneous hot flow anomalies at quasi-parallel shocks: 1. Observations. *Journal of Geophysical Research (Space Physics)*, 118(6):3357–3363, Jun 2013.